OBSERVATIONS OF INERTIAL OSCILLATIONS DURING THE NANTUCKET SHOALS FLUX EXPERIMENT

by

Tamara M. Wood

B.S.M.E., Union College

(1982)

SUBMITTED TO THE DEPARTMENT OF EARTH,
ATMOSPHERIC AND PLANETARY SCIENCES
IN PARTIAL FULFILLMENT OF
THE REQUIREMENTS OF THE DEGREE OF

MASTER OF SCIENCE IN PHYSICAL OCEANOGRAPHY

at the

MASSACHUSETTS INSTITUTE OF TECHNOLOGY

January 1987

Signature of Author_____
Department of Earth, At[illegible]d Planetary Sciences

Certified by_____
David C. Chapman
Thesis Supervisor

Accepted by_____
W. F. Brace
Chairman, Departmental Graduate Committee

TABLE OF CONTENTS

OBSERVATIONS OF INERTIAL OSCILLATIONS

DURING THE NANTUCKET SHOALS FLUX EXPERIMENT

by

TAMARA M. WOOD

Submitted to the Department of Earth, Atmospheric and Planetary Sciences
in partial fulfillment of the requirements for the Degree of
Master of Science in Physical Oceanography, January 1987

ABSTRACT

The current spectra from an array of current meters aligned approximately North-South across the shelf break south of Nantucket Island show a prominent peak in the clockwise-rotating component of the kinetic energy in the inertial frequency band, indicating that inertial oscillations are an important component of the internal wave field over the shelf.

The near-inertial energy is highly surface-intensified and for the most part is associated with generation at the surface by local winds. There is one event in the time series of the inertial energy which appears to have propagated into the array from offshore of the shelf break, but in general the influence of the ocean seaward of the shelf break is minimal.

The vertical structure of the near-inertial motions is well-resolved and appears to be dominated by a first baroclinic mode. However, the horizontal scale is ambiguous because the mooring spacing does not resolve the high wavenumber end of the range of possible values. Therefore, the observed response could result from small scale (O(20 km)) horizontal variability in the wind stress or from a large scale (O(200 km)) barotropic wave reflecting from the coast. The two possibilities cannot be distinguished by the available data. Variability in the mean geostrophic currents may also be an important factor in determining the horizontal scale.

Thesis Supervisor: Dr. David C. Chapman

Title: Assistant Scientist

I. Introduction and Historical Review

The present work is primarily a description of the spatial and temporal structure of the energy in the near-inertial frequency band over a continental shelf. Motions at these frequencies, referred to as inertial oscillations or near-inertial waves, have been established as an important contribution to the total internal wave spectrum in the deep ocean. The canonical Garrett and Munk spectrum, for example, allows for a peak in the energy at the local inertial frequency (Garrett and Munk, 1979). It is therefore appropriate, as a prelude to examination of inertial oscillations over a continental shelf, to review some observed characteristics of near-inertial frequency motions in the deep ocean away from bottom and lateral boundaries. The effects of these boundaries on the motions over the continental shelf can then be anticipated and this should aid in the interpretation of the observations over the shelf. Also, consideration must be given to the inertial wave field in the deep ocean as it will determine the boundary condition at the open boundary over the shelf break which separates the shelf and deep water regimes. With these goals in mind some observations in the open ocean will be presented, and for the purposes of discussion there are three categories: (1) observations in and immediately below the surface mixed layer where the inertial oscillations are most energetic and where the transition between direct forcing by the wind and free propagation takes place, (2) observations below the mixed layer and through the main thermocline to a nominal depth of 3000 m characterized by a dominantly downward propagation of energy, and (3) observations at depths nominally 3000 m to

the bottom where the total energy level in the inertial band is lowest and the dominance of downward propagation of energy is reduced.

Observations in the surface mixed layer at site D (39°10'N,70°W) have been presented by Pollard (1970, 1980). The data were taken during the summer of 1970 from a triangular array of three moorings separated by 50-70 km and instrumented at 12, 32, 52 and 72 m. The total inertial energy at all the moorings is approximately the same at the 52 and 72 m levels, but increases through the 32 m level to the surface, being 2 to 5 times higher at the 12 m level. The current records at the 12 m level are highly coherent over the separation of the moorings: coherence/phase calculations as well as a complex demodulation analysis give phase differences between instruments which are consistent with 700-1700 km horizontal wavelengths. The horizontal coherence scale drops off with depth: the currents are somewhat coherent at 32 m but at 52 and 72 m depth there is no coherence over the distance between the moorings. During times of active surface generation of inertial oscillations the phase progression is upward such that energy is propagated downward out of the generation region. A picture emerges of a surface region forced by local winds at the ocean/atmosphere interface, which results in a surface-intensification of energy and horizontal coherence scales which decrease from the large scale of meteorological forcing at the surface to smaller scales within a few tens of meters, presumably because waves with smaller horizontal scales propagate vertically more rapidly. Coherence calculations in the vertical indicate that the near-inertial energy is characterized by a small aspect ratio: vertical coherences over the 20 m distance between current meters at a single mooring are

high, with phase differences indicating that the vertical wavelength of the motion is from 100-240 m. This is slightly larger than the estimate of Webster and Fofonoff (1967) (see also Webster, 1968) who found, using a different data set from site D, that currents at 90 m depth were coherent over a 3 km horizontal separation but that currents at 7 and 88 m on the same mooring were incoherent. However, both estimates show that horizontal wavelengths are at least an order of magnitude greater than vertical wavelengths.

Below the mixed layer and through the main thermocline there is more evidence of the propagation of the wind-forced energy out of the mixed layer. Fu (1981) documents the characteristics of inertial oscillations in the POLYMODE data in the North Atlantic. POLYMODE data suitable for calculating vertical coherence scales were available over depths from 88 to 1500 m, from which he calculates a vertical coherence scale on the order of 200 m. There is also evidence of upward phase propagation in the POLYMODE data which is associated with downward energy propagation of internal waves. Additional evidence of upward phase propagation through the thermocline and down to ~3000 m depth is given by Sanford (1975), Leaman and Sanford (1975), and Leaman (1976), using velocity-with-depth profiles collected as part of MODE 1. The upward phase propagation is deduced from spectral analysis techniques, including a dropped lagged rotary coherence over the horizontal wavenumber (Sanford, 1975) and a rotary wavenumber spectrum (Leaman, 1976). Visual inspection of the MODE 1 velocity-with-depth profiles indicates that much of the energy is contained in vertical wavelengths on the order of 100-200 m through the thermocline and 300-500 m below, consistent with the observation of Leaman and Sanford (1975) that a WKB type of scaling in which the vertical wavelength is inversely proportional to N is appropriate.

Estimates of the horizontal coherence of near-inertial waves in the main thermocline indicate that the horizontal scale does not decrease rapidly with depth. The POLYMODE data between approximately 200 and 600 m depth show horizontal coherence scales from 50 to 70 km (Fu, 1981). This probably represents an upper bound on the horizontal scales -- results documented by Webster (1968) from the Sargasso Sea show that currents at 617 m are not coherent with currents at the same depth on a mooring 64 km away. To summarize the observations through the main thermocline to about 3000 m depth, the data indicate that below the mixed layer energy propagates downward in the form of near-inertial internal waves with horizontal wavelengths on the order of tens of kilometers and vertical wavelengths on the order of hundreds of meters.

Observations between 3000 and 6000 m are more limited, but deep water data from POLYMODE (Fu, 1981) show that at these depths there is significant coherence in the vertical even over distances of about 1000 m. The phase information cannot be used to estimate a vertical wavelength consistent with a WKB scaling of values calculated at shallower depths, and Fu concludes that a standing wave type of response dominates, with a horizontal coherence scale that appears to be reduced from that through the thermocline. This requires an equipartition of upward and downward propagating energy, but Sanford (1975) suggests that in the MODE 1 velocity profiles the energy in the deep water may be propagating downward along characteristics. In reality both features are probably present at all depths, and the decrease in the dominance of downward-propagating energy below 3000 m allows the standing wave to be seen more easily. Other evidence of a modal structure has

been found in the Mediterranean (Perkins, 1972) where the stratification is such that only a few vertical modes are needed to represent the structure. Because the current structure is quite simple, the vertical mode is more easily observed than in the Sargasso Sea where most observations have been made.

The summary of observations presented thus far is not complete but it is representative of the historical work. Fu (1981) offers an interpretation of the total near-inertial field as a sum of a global and a locally forced response. The inertial waves in the upper part of the water column are forced by the local wind at the surface and propagate energy downward through the thermocline. This locally forced wave field is also the most energetic; in the POLYMODE data it has energy peaks at the inertial frequency more than twice those found at greater depths. In regions unaffected by local forcing, a relatively less energetic global wave field dominates, consisting of internal waves which are remotely generated at lower latitudes and propagate to their turning latitudes where they become by definition inertial waves. Near their turning latitude, the velocity wave functions interfere constructively and a prominent peak slightly above the local inertial frequency appears in the energy spectrum (Munk and Phillips, 1968). This global wave field is dominated by low vertical wavenumbers because such waves can propagate large distances without being dissipated by viscous effects, and they undergo nearly perfect reflection at the bottom boundary layer in the absence of topographic features. The global wave field also explains the appearance of a standing wave at great depths.

There are two questions to be asked given what is known about the behavior of the near-inertial wave field in the deep ocean. First, how does

the shelf environment change the behavior of the near-inertial wave field? Second, how, if at all, does the wave field in the deep ocean affect the wave field over the shelf through the open boundary at the shelf break? Each of these questions can be briefly addressed given the existing literature, although the conclusions are speculative.

In response to the latter question, the open boundary at the shelf break allows for the possibility of propagation of inertial energy onto the shelf from the deep ocean. In analogy with Fu's (1981) interpretation, consider a deep ocean inertial-internal wave field, incident upon the shelf/slope region, which is comprised of a global wave field generated far from the continental slope/continental rise region and a wave field generated locally at the surface. Figure 1.1 shows schematically the shelf and deep ocean domains, the principle components of the deep ocean inertial wave field, and the relevant length scales.

The global wave field is not expected to transfer significant energy onto the shelf. The field has travelled far from its source and due to dispersive and viscous effects it is dominated by low vertical modes. Its vertical length scale L, which is a significant portion of the deep water depth D, is much greater than the depth of the shelf d. Thus the shelf break open boundary is a very small opening in the continental slope, which acts as a vertical wall to the global near-inertial wave field since the slope is generally supercritical to these frequencies at the latitudes of interest; that is, the continental slope is steeper than the slope of near-inertial characteristics, so incident energy is reflected back into the deep ocean rather than being transmitted up the slope. More important,

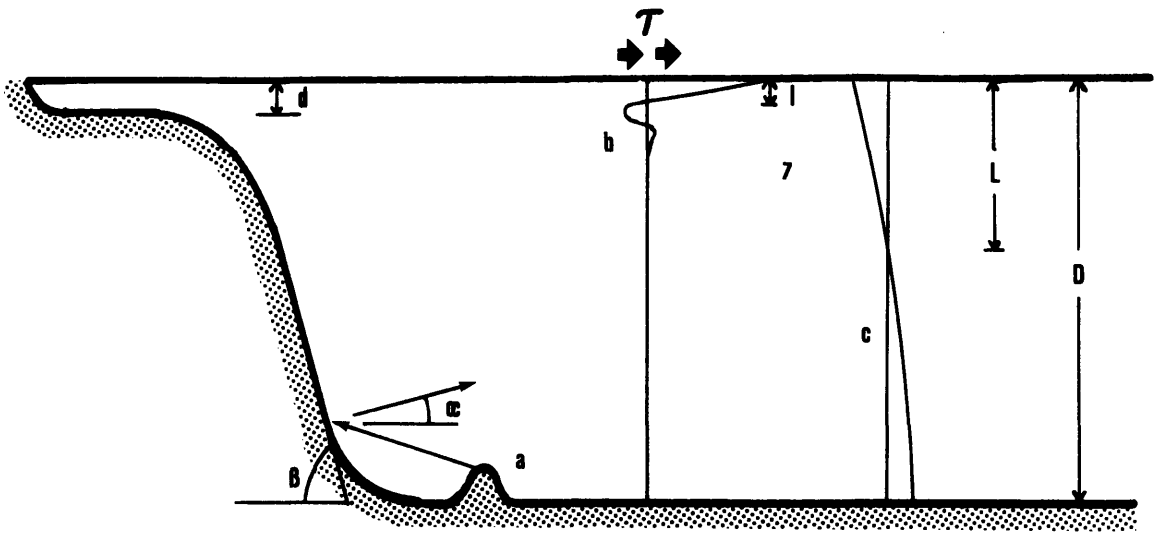

Figure 1.1: Schematic of the continental shelf and deep ocean regimes showing the relevent vertical length scales and three possible contributions to the deep ocean near-inertial wave field: (a) intensification upon bottom reflection, with energy concentrated along characteristics with slope α, where $\alpha << ß$, (b) surface generation by winds with energy surface-intensified and concentrated in length scales comparable to the depth of the shelf d, and (c) the global wave field with energy in low vertical wavenumbers such that the vertical length scale $L \sim D >> d \sim \ell$.

however, is the fact that any energy that is transmitted should be insignificant, since the amount of energy in the global wave field is a small contribution to the total energy in the regions of strong local forcing near the surface (Fu, 1981).

The surface-generated wave field is surface-intensified and contains energy in vertical scales ℓ comparable to or smaller than the depth of the shelf d, so that it is possible that such a wave field incident on the shelf could transmit significant energy. The limiting factor in this transmission will be the slow horizontal group velocity of near-inertial waves. For instance, a wave with a horizontal wavelength of 50 km and a frequency 3% above f has a vertical wavelength of 150 m as calculated from the dispersion relation and a horizontal group velocity $c_{gH} = N^2k/\omega m^2$ of 14 cm/s, using $f = 9.4 \times 10^{-5} s^{-1}$ and $N^2 = 2 \times 10^{-4} s^{-2}$. Horizontal group velocities of this magnitude will restrict the area seaward of the shelf break which can affect the shelf through the open boundary to distances within a few days travel time of the shelf break. Waves with larger horizontal wavelengths at the same frequency will travel faster, but the vertical wavelengths become larger as well and transmission of energy across the shelf break will be inhibited. It is reasonable to conclude that near-inertial energy propagating onto the shelf from the deep ocean probably originated within a distance of a few hundred kilometers from the shelf break, so that the atmospheric disturbances responsible should be easy to identify.

One other possibility that should be considered is that near-inertial energy may be amplified upon reflection at the bottom or a topographic feature where the slope is nearly equal to the characteristic slope (Eriksen,

1982). Downward-propagating waves are reflected into upward-propagating waves with smaller vertical wavelengths and smaller group velocities. Energy density will be greater in the reflected waves due to the requirement of zero energy flux normal to the bottom. Few observations of such a wave field exist, but Kunze and Sanford (1986), for example, observed upward-propagating near-inertial waves over Caryn Seamount (36°40'N, 68°W). The energy was most intense along near-inertial characteristics emanating from the summit. The slope of the near-inertial characteristics is given by $\alpha^2 = (\omega^2 - f^2)/N^2$. At 40°N latitude near the bottom where a reasonable value for the buoyancy frequency is $2 \times 10^{-3} s^{-1}$, the slope of the characteristics of a wave of frequency 1.01f will be $\alpha = 7 \times 10^{-3}$. At shallower depths the slope of the characteristics is smaller due to the increased buoyancy frequency (see Appendix). A reasonable value for the bottom slope over the continental slope south of Nantucket Island is ~.05, confirming that at mid-latitudes the slope can be considered supercritical to near-inertial waves; that is, inertial energy originating at the bottom and propagating shoreward along the characteristics will be reflected back into the deep ocean and should not be important when considering the transfer of inertial energy across the shelf/slope boundary.

What does the deep ocean internal wave field suggest about the behavior of the near-inertial energy over the shelf? The observations presented show that a region of strong surface forcing in the deep ocean will propagate energy downward out of the mixed layer and well into the thermocline. Because outer shelf depths are on the order of 100 m it seems likely that the bottom boundary will interfere with the vertical propagation of energy,

reflecting energy back to the base of the mixed layer and setting up a strongly modal response. There is, in fact, observational evidence of a modal response over the shelf. Mayer et al. (1981) observed a first baroclinic mode structure at two moorings along the 70 m isobath in the New York Bight. Following the passage of a hurricane over the site, near-inertial frequency motions were set up such that currents in the upper portion of the water column were 180° out of phase with currents in the lower portion of the water column. There was also some indication of a second vertical mode at two mid-shelf locations (55 m depth), but the motions were heavily damped and disappeared quickly. Vertical displacements were in phase through the water column and temperature excursions of 4°C at the middle portion of the water column indicated a strong internal mode. Additional observations of a first vertical mode were made in the North Sea (80 m depth) by Schott (1971), who found that instruments above and below the thermocline at the same mooring were 180° out of phase, while the temperature fluctuations were in phase over the entire water column. Maximum vertical amplitudes of 1 m were found near the thermocline, again indicating a strong internal response.

In the open ocean, inertial energy is dispersed out of the mixed layer when a wind stress curl creates a divergence of the mixed layer currents, which in turn creates vertical velocities at the base of the mixed layer, or Ekman pumping (Gill, 1984). In a coastal environment surface layer divergence can be provided by the coastline, even in the absence of a wind stress curl. A horizontally uniform wind blowing in the presence of a coast produces inertial currents everywhere in the surface mixed layer, but due to

the requirement of no normal flow, waves are reflected at the coast and propagate away. Millot and Crepon (1981) have interpreted a two-layer structure in the inertial response to upwelling-favorable winds in the Gulf of Lions as due to the arrival of waves generated to satisfy the boundary condition at the coast. The upper layer currents, which are presumably dominated by the directly wind-driven response, are coherent over all the moorings with no statistically significant phase difference. The lower layer currents and the temperature signals are not coherent over all the moorings because they contain contributions from waves propagating from different directions, always perpendicular to the coast where they originated.

Not all observations of inertial oscillations over the shelf show a vertical structure that is dominated by a first baroclinic mode. Kundu (1976) examined data at one mooring in 100 m of water off the coast of Oregon where the shelf has a much steeper slope than the Mid Atlantic Bight. Eleven current meters were spaced from 2 to 20 m apart, and a calculation of the lagged correlation of the band-pass filtered time series shows a systematic clockwise rotation of the current vector with depth, consistent with upward phase propagation and downward energy propagation. The cyclesonde measurements of Johnson et al. (1976) in the same area also show an inertial event propagating phase upward from about 70 m to about 20 m depth. These observations are consistent with theoretical work which predicts that over a strongly sloping bottom the flat-bottom modes are distorted such that there is a continuous change of phase with depth and energy is propagated vertically (Wunsch, 1968, 1969; and Lai and Sanford, 1986).

Having given some consideration to the effects of the lateral and bottom boundaries of the continental shelf on the inertial wave field over

the shelf, and compared some of these ideas with existing observations, it is appropriate to ask what new information can be gained from the data set under consideration. The data are current meter records from an array of six moorings aligned approximately North-South across the outer shelf south of Nantucket Island (see Section II). The horizontal spacing of the moorings is on the order of 20 km and the vertical spacing of the current meters on the order of 20 m, representing relatively dense spacing in two dimensions. The time series extend over a period of one year, covering all seasons.

One of the questions that has not been resolved by existing observations is the horizontal scale of inertial oscillations over the shelf. Estimates vary from 300-700 km (Thomson and Hugget, 1981) to 20-50 km over an array off the coast of Oregon (Anderson et al., 1983). In both of these cases, the average horizontal wavelength more than doubled from one major inertial event to another leading to the conclusion that the "wavelength is the result of the particular circumstances generating the motion, rather than of the oceanic environment" (Anderson et al., 1983). Given that this is the case, the year-long records from the Nantucket Shoals Flux Experiment (NSFE) may yield a range of wavelengths appropriate to the forcing functions of the Middle Atlantic Bight to complement the estimate of 280 km given by Mayer et al. (1981).

The vertical structure of the inertial response appears to be related to the particular environment; i.e. to the slope of the bottom and to the stratification. The observations to date indicate that in the cases where coherent inertial energy extends through the water column, a gentle slope

will result in a standing wave type of response and a strong slope causes a vertical propagation of energy. The NSFE current meter records should establish whether the bottom slope, in combination with the stratification particular to this region at various times of the year, causes a strong vertical propagation of inertial energy or if the flat-bottom type of response still dominates. Existing observations do not show how the vertical structure may vary along a transect perpendicular to the coast from the shelf break into shallower water. The NSFE array should provide a continuous picture of the vertical structure from the shelf break toward the coast over approximately 100 km.

Finally, while the wind has been established as the primary source of inertial energy (Pollard and Millard, 1970), at least near the surface, many authors remark on the failure of some events in the inertial energy to correlate with events in the wind records (e.g. Anderson et al., 1983; and Kundu, 1976). The NSFE array, which is positioned across the shelf break, should be helpful in addressing the question of whether or not the open boundary at the shelf break can act as a source for the near-inertial wave energy on the shelf. If near-inertial waves over the shelf can originate in the deep ocean, then this may account for some events in inertial energy which are not forced by the local winds.

II. Description of the Data Set

A complete description of the NSFE field program is contained in Beardsley et al. (1985), and here only the aspects of the measurements which will be useful in understanding the analysis to follow will be presented.

A six-element linear array of moored instrumentation was deployed in NSFE along the transect shown in Figure 2.1 across the continental shelf and upper slope south of Nantucket Island. The mooring transect was oriented approximately perpendicular to the local middle and outer shelf isobaths. The six mooring locations (designated N1-N6) were separated horizontally by 16-23 km and were located in water of depth ranging from 46 m at N1 to 810 m at N6. A cross section of the array indicating the positions of 19 vector averaging current meters (VACMs) is also shown in Figure 2.1. Note that the depth of the instrument is indicated in parentheses next to the mooring designation, e.g. N6(10) is the instrument at 10 m depth at mooring 6.

NSFE was designed as a one-year field experiment, with most of the instrumentation deployed for two periods of approximately six and seven months duration. This breaks the data set up naturally into two periods, summer and winter, lasting from March 1979 to September 1979 and from October 1979 to March 1980, respectively. Longer-term measurements were made at mooring 2 by the United States Geological Survey so that it was maintained on a different deployment and recovery schedule. As a result the time series at mooring 2 are broken during August 1979 and again during December 1979. A summary of the good current meter data returned is shown

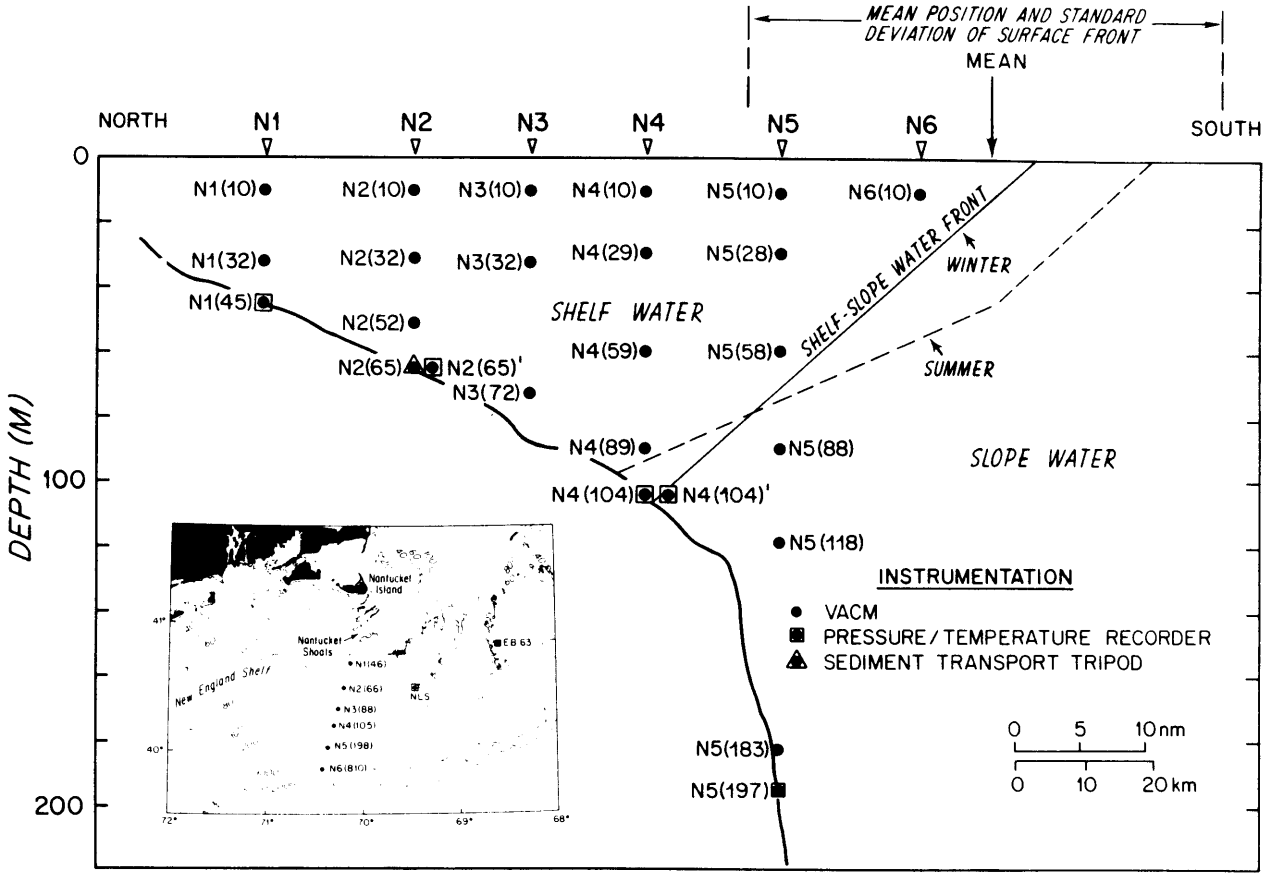

Figure 2.1: Schematic cross section of the NSFE moored array. The water depth in meters appears in parentheses next to the mooring number for each instrument. The insert map shows the locations of the NSFE array and the two meteorological stations, the Nantucket Light Ship (NLS) and NOAA environmental buoy (EB63). The local water depth at each mooring is shown in parentheses next to the mooring number (from Beardsley et al., 1985).

in Figure 2.2. During the summer period of NSFE, 16 out of 19 current meters returned good current data. During the winter period only 10 of 19 returned good current data because of increased instrument failure and mooring losses. The currents will be analyzed in an alongshelf (roughly east) and cross-shelf (roughly north) coordinate system aligned with the local shelf topography: the positive alongshelf component is directed towards 107°T (perpendicular to the moored array transect) and the positive cross-shelf component toward 17°T (parallel to the moored array transect).

Wind measurements were routinely made every three hours at the Nantucket Light Ship (NLS) located at 40°30'N, 69°30'W throughout most of NSFE (see insert in Figure 2.1). An edited version of this time series was then used to estimate surface wind stress using the neutral steady-state drag coefficient and iterative method given by Large and Pond (1981). A gap from 18 April to 9 May 1979 in the NLS wind stress time series was filled with surface stress values computed using wind data collected by the NOAA environmental buoy EB-63 located at 40°41'N, 68°30'W. This procedure was used because the two meteorological stations were closely spaced in relationship to the dominant scales of surface wind variability and excellent agreement was found between the two wind-stress time series computed for an overlapping period when both stations were working.

As part of the field program, a total of 27 hydrographic cruises were made along the moored transect. The hydrographic observations were obtained with XBTs, CTDs and/or water bottles with reversing thermometers. The sections are presented by Wright (1983).

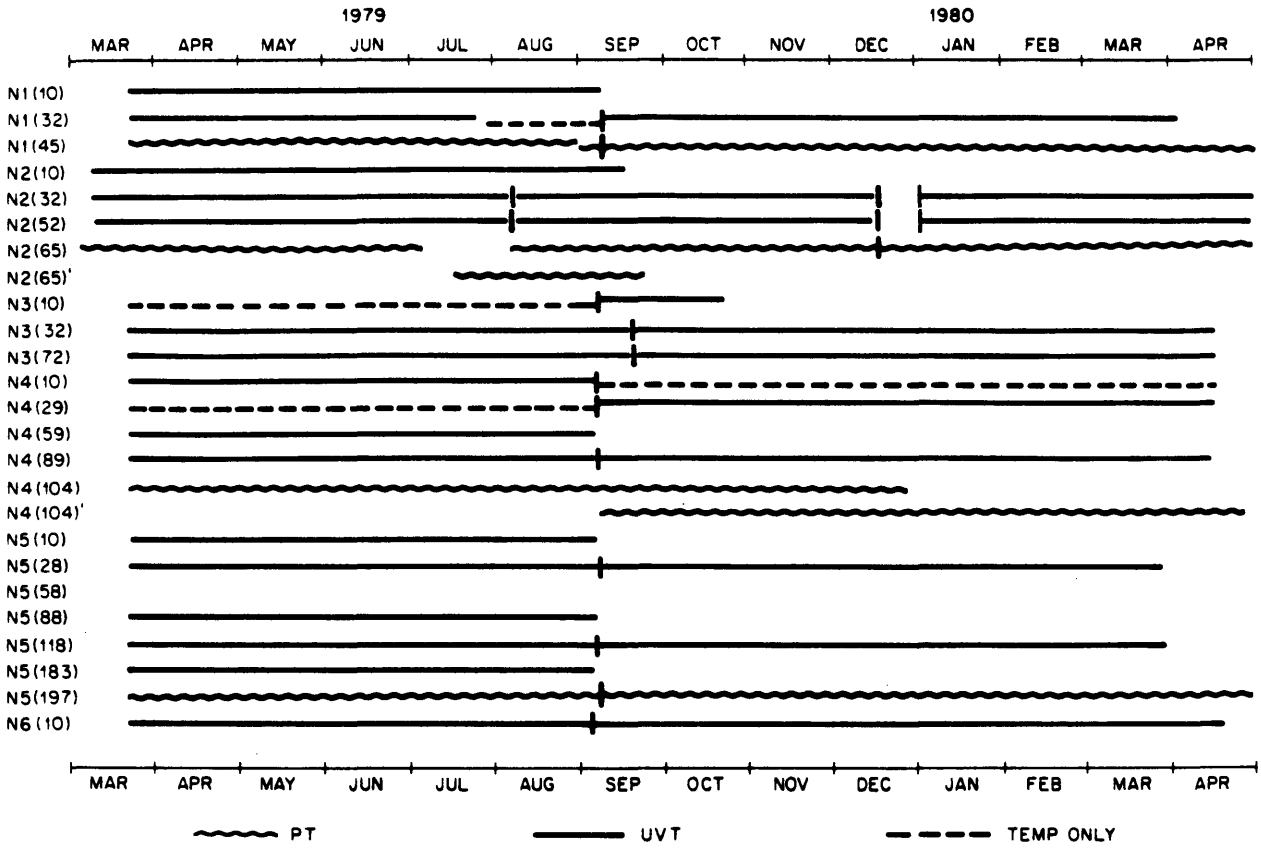

Figure 2.2: Summary chart of good current return (from Beardsley et al., 1985).

III. Analysis of the Data

The analysis of the current meter data is presented in the following sequence. First, the average energy in the inertial frequency band over the entire time series of the summer and winter periods is calculated at each instrument in the form of rotary spectra. The time dependence of this energy is then examined using a least squares technique over small segments of the time series. Horizontal propagation and wavelength are investigated using phase differences across the array arising from coherence calculations and the least squares technique. The coherent energy over the array is then represented in a concise form using an empirical orthogonal function analysis, and the time dependence of the dominant mode is examined in order to determine whether averaging over the entire time series gives useful information about the coherent energy in individual energetic events at near-inertial frequencies. Finally, a summary is presented in order to focus attention once again on the specific questions posed in the introduction.

A. Rotary Spectra

Rotary spectra (Gonella, 1972) were used to separate the kinetic energy in the clockwise-rotating component from that in the counterclockwise-rotating component. The near-inertial frequency currents can be represented as the sum

$$u + iv = A(x,y,z)e^{i(f+\varepsilon)t} + B(x,y,z)e^{-i(f+\varepsilon)t} ,$$

where u and v are orthogonal velocity components, f is the local inertial frequency, ε is the small deviation from this frequency, A and B are

complex amplitudes, and x, y and z are directional coordinates. If B >> A then the particle trajectories approximate clockwise circles and the currents are associated with inertial oscillations.

Several spectra for the summer and winter periods at N4 are shown in Figure 3.1. The clockwise-rotating component has a sharp peak at the inertial frequency (~.054 cph) and amplitudes 10 to 100 times greater than the counterclockwise-rotating component, indicating a significant amount of kinetic energy in near-inertial oscillations. These spectra are representative of the results over most of the array. During the summer period the energy density is very surface-intensified, dropping by more than 75% from N4(10) to N4(59). The surface intensification is reduced during the winter period; there are no data at N4(10), but there is only a small decrease in energy density between N4(29) and N4(89). A summary of the clockwise spectra over the array during each period is given in Table 3.1. The winter data are limited at the surface, but at N6(10) the kinetic energy is reduced during the winter period. Comparisons are possible at N4 and N5 only for instruments deeper than 10 m, and the kinetic energy is increased during the winter period. At N1 and N2 the energy in general decreases during the winter period. Note that the comparison is complicated by the fact that at N2 the first "winter" time series actually contains the last part of the summer time series at the other instruments.

The temperature spectra show small peaks near the inertial frequency at N5(118), N5(183), N3(10), N3(32), N4(10) and N4(89) during the summer and at N4(29) and N4(89) during the winter. None of these peaks is significant at 95% confidence.

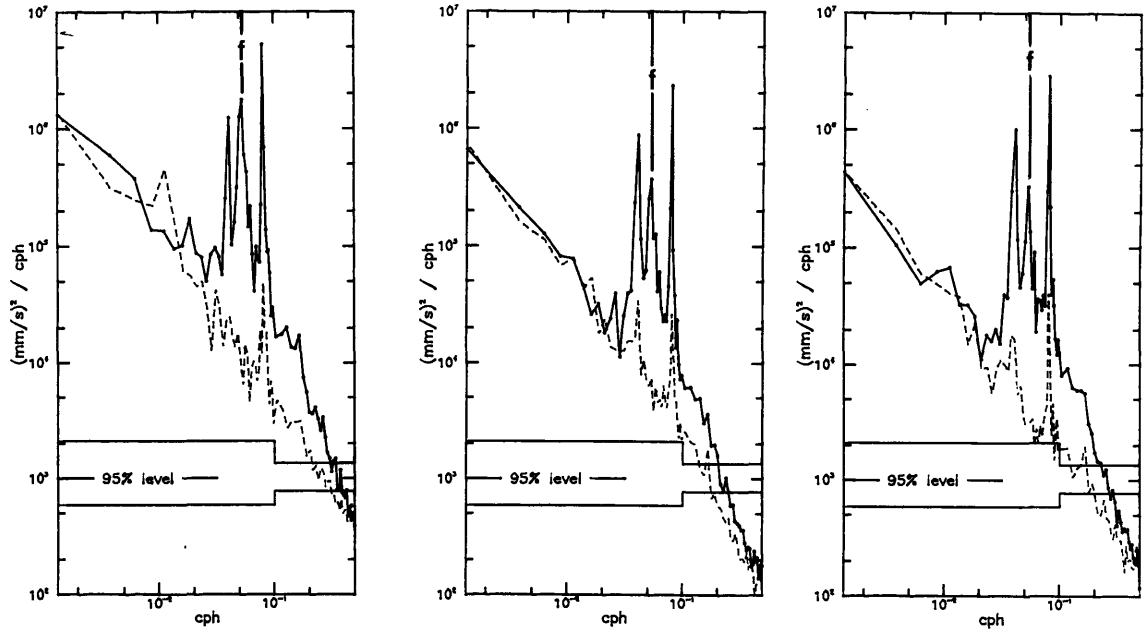

N4(10) N4(59) N4(89)

a.

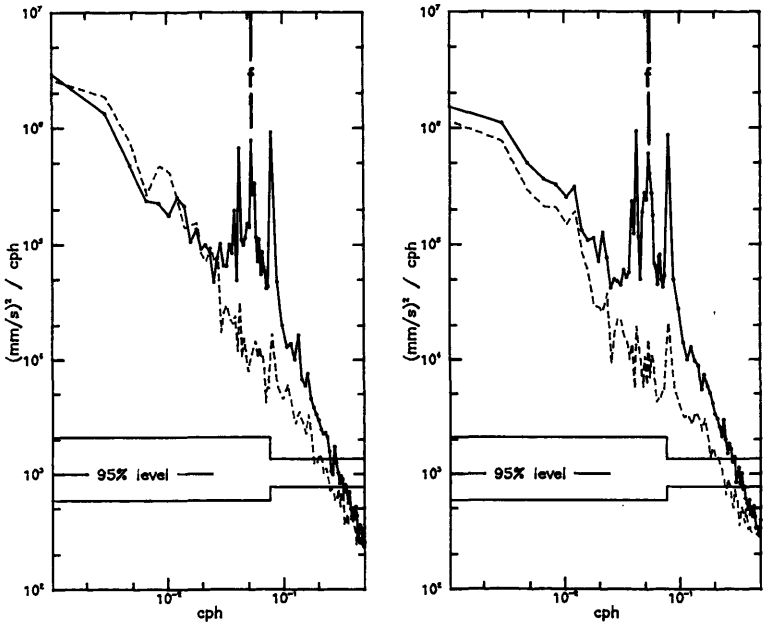

N4(29) N4(89)

b.

Figure 3.1: Rotary spectra for (a) the summer period and (b) the winter period at mooring 4. The clockwise rotating energy is indicated by the solid line, counterclockwise by the ashed line. Estimates in the inertial frequency band are averaged over ten frequency bands with a bandwidth of ~.18 - .25 x 10^{-3} cph. The inertial frequency is labeled "f".

B. Complex Demodulation

A complex demodulation technique was used to analyze the time dependence of the near-inertial energy. This was considered a good technique to use in this case because the signal of interest is peaked in a very narrow band, making the expansion in a sinusoid of a single frequency somewhat realistic. Since the array is aligned nearly north-south, the inertial frequency varies from 0.0535 to 0.0545 cph from N6 to N1. The frequency used in the complex demodulation was 0.054 cph, the average over the array.

The complex demodulation was carried out as follows. Over an interval of time T equal to approximately 10 inertial periods (180 hours), the time series is approximated by the two-term expansion

$$U(t) = a_1\cos(ft) + a_2\sin(ft). \tag{3.1}$$

It is desired that this two term expansion represent the time series as well as possible (in a least squares sense) over the interval T. This is done by minimizing γ, where γ is given by

$$\gamma = \sum_{i=1}^{N} [u(t_i) - U(t_i)]^2 \tag{3.2}$$

where N is the number of data points in T and $u(t_i)$ is the observed signal. The summation above is a function of a_1 and a_2, therefore minimizing it requires

$$\frac{\partial}{\partial a_j} \left\{ \sum_{i=1}^{N} [u(t_i) - U(t_i)]^2 \right\} = 0 \ , \ j=1,2. \tag{3.3}$$

This is a system of two equations in the two unknowns a_1 and a_2. Interchanging the differentiation and summation, (3.3) becomes

$$\begin{aligned} &\sum_{i=1}^{N} [u(t_i) - a_1\cos(ft_i) - a_2\sin(ft_i)] \cos(ft_i) = 0 , \\ &\sum_{i=1}^{N} [u(t_i) - a_1\cos(ft_i) - a_2\sin(ft_i)] \sin(ft_i) = 0 , \end{aligned} \tag{3.4}$$

or, in matrix form,

$$\underline{a} = (\underline{\Gamma}'\underline{\Gamma})^{-1}\underline{\Gamma}'\underline{u} \tag{3.5}$$

where $\underline{u}$ is the column vector of the data,

$$\underline{a} = \begin{Bmatrix} a_1 \\ a_2 \end{Bmatrix} , \quad \underline{\Gamma} = \begin{Bmatrix} \cos(ft_1) & \sin(ft_1) \\ \cdots & \cdots \\ \cos(ft_N) & \sin(ft_N) \end{Bmatrix} ,$$

and $\underline{\Gamma}'$ is the transpose of $\underline{\Gamma}$.

After solving for the coefficients a_1 and a_2 a new segment of the time series of length T is chosen, starting a period of time Δ after the start of the last segment. The procedure is repeated and new estimates of a_1 and a_2 are calculated. In this case a Δ of approximately one inertial period (18 hours) was chosen so that the segments of the time series overlap and the resulting correlation between adjacent points causes some smoothing. At points separated by Δ an estimate of the amplitude $A = (a_1^2 + a_2^2)^{1/2}$ is obtained, creating a new time series representing the amplitude of only that portion of the observed time series which is oscillating near the inertial frequency. The rate of change of the phase, $\theta = \tan^{-1}(a_2/a_1)$, is an indication of how closely the observed frequency matches the demodulation

frequency f. An increasing phase indicates that the observed frequency is slightly subinertial; a decreasing phase indicates that the observed frequency is slightly superinertial.

The segment length T used here is long compared to that chosen by other authors. For example, Pollard (1980), Perkins (1970), and Pettigrew (1981) used a segment length T equal to two inertial periods; Hayes and Halpern (1976) and Johnson (1981) used a segment length T equal to two days. As pointed out by Kundu (1976), however, contamination by the tides can be a problem. A long segment was used here to decrease the admission of tidal energy. Assume for demonstration purposes that the length of time $T = N\delta t$ (δt is the sampling interval) is an even number of inertial periods. Then equations (3.4) can be written as

$$a_1 = \frac{2}{N\delta t} \sum_{i=1}^{N} u(t_i) \cos(ft_i)$$

$$a_2 = \frac{2}{N\delta t} \sum_{i=1}^{N} u(t_i) \sin(ft_i). \qquad (3.6)$$

The complex demodulation is now identical to computing Fourier coefficients at the inertial frequency over the segment T, the weighting function being a boxcar of length T and unit height. In the frequency domain the corresponding spectral window is $\sin(2\pi(\omega-f)T)/2\pi(\omega-f)T$ (Perkins, 1970), where ω is the variable frequency and f is the demodulation frequency. For the segment length T used here this window admits about 7% of the K1 and 3% of the M2 tidal amplitude. If, for example, a segment length T equal to approximately two inertial periods is used (36 hrs), then 14% of the K1 and

5% of the M2 tide is admitted. Because of the large tidal peaks in Figure 3.1, even with the long piece length used here the leakage of tides may not be negligible, especially at the moorings closest to the shore where the tidal amplitudes are greatest.

Figure 3.2 shows the results of a complex demodulation over the summer period at N6(10). Three criteria should be used in determining when the amplitude represents a true inertial signal. First, the amplitude must be distinguishable from the background noise level. Second, the phase must be relatively stable, indicating that the demodulated signal is in the near-inertial band. Third, the amplitude of the east and north components must be equal with a phase difference between them of 90 degrees, consistent with particle motion which is approximately circular. Figure 3.2 shows that the east and north components are nearly equal over most of the time series; this is representative of the results at the other instruments. The noise level calculated from the energy in the tides at N6(10) using the spectral window described above and the amplitude of the tidal peaks is indicated by the solid line. The periods of highest amplitude are characterized by a phase difference between the two components (denoted PHSD) of nearly 90 degrees, and a change in phase which is relatively small. For example, between 30 April and 9 May the change in phase is about 120 degrees, corresponding to a frequency about 3% below the demodulation frequency, well within the bounds of the inertial band.

Assurance is needed that, even though a particular event in the amplitude of the complex demodulate satisfies the criteria for a "true" inertial signal, the event is not simply due to the fortuitous superposition of

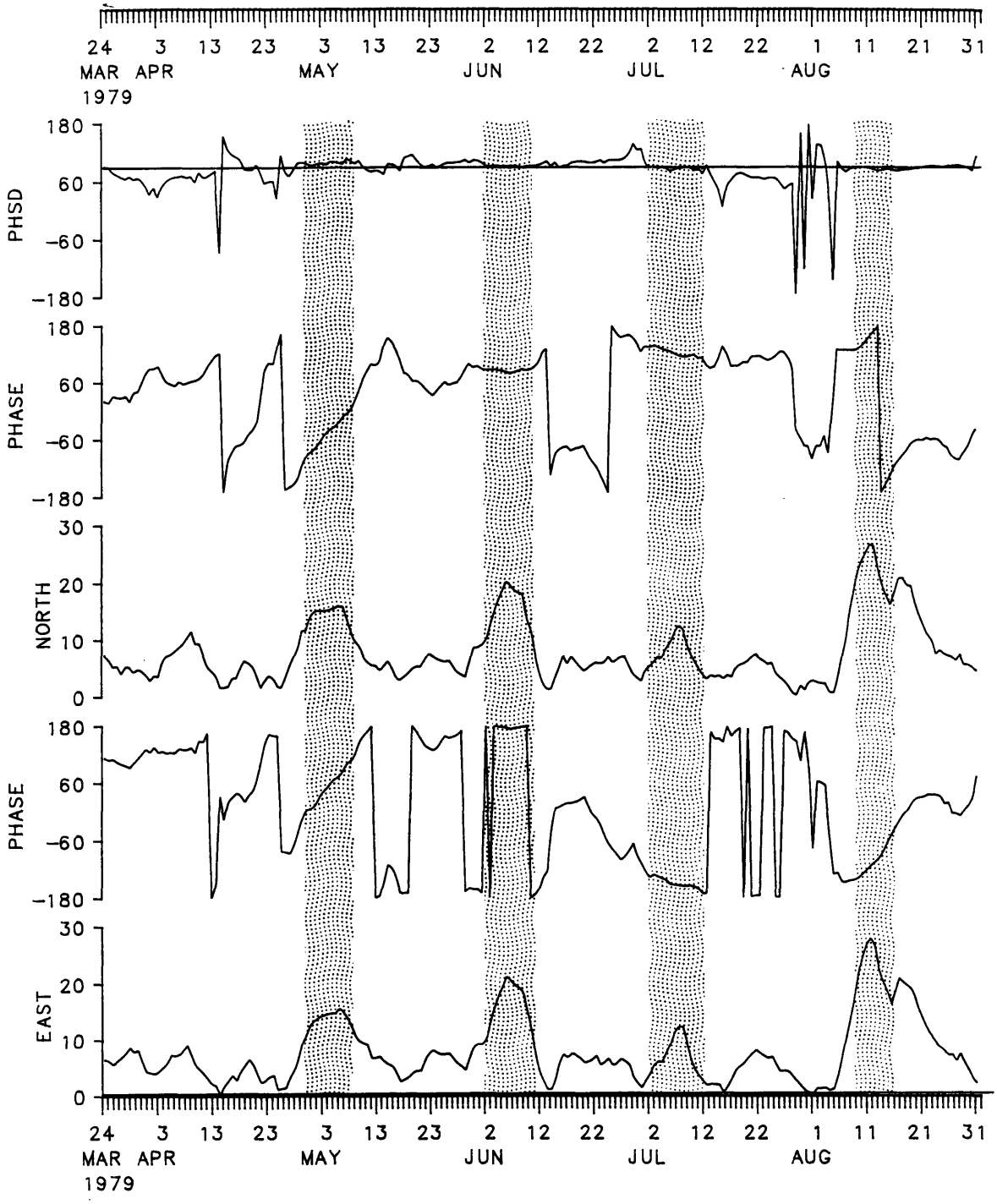

Figure 3.2: Results of a complex demodulation at the frequency f = 0.054 cph on the time series at instrument N6(10), summer period. The units of amplitude are [cm/s]. Amplitude and phase are shown for east and north components, and the phase difference between the two components is denoted PHSD. The solid line on the PHSD axis indicates 90°.

signals in a time series which is really nothing but white noise. To investigate this possibility, a complex demodulation analysis was performed exactly as described above on a time series of random numbers generated with the same range of values as the current data at N6(10). The resulting time series of amplitude and phase are shown in Figure 3.3. Note that the random events in this time series are limited in amplitude to about 10 cm/s. In Figure 3.2 the events with amplitude greater than 10 cm/s are indicated; it should be noted that these events are also clearly visible in a detided version of the original time series of the the current at N6(10).

Figure 3.4 shows the time series of the complex demodulates for the east component of velocity (that for the north component being nearly identical) for the summer period at all moorings. On each time series a noise level is indicated; this noise level was calculated from the energy in the K1 and M2 tides using the spectral window described above. Note the high visual horizontal correlation between instruments at N4, N5 and N6, especially at 10 m depth. There is also some indication of vertical correlation at N3, N4 and N5, even though amplitudes decrease substantially below 10 m depth.

The correlation among the 10 m instruments is dominated by the same four events which were indicated in Figure 3.2. These events can be clearly picked out at N4, N5 and N6, and event 4 is seen also at N2, perhaps even at N1. Each event satisfies the three conditions stated above for being a true inertial signal. This was determined in a qualitative manner similar to that described for N6(10). First, a minimum level of significance for the complex demodulate amplitudes was determined by calculating the leakage

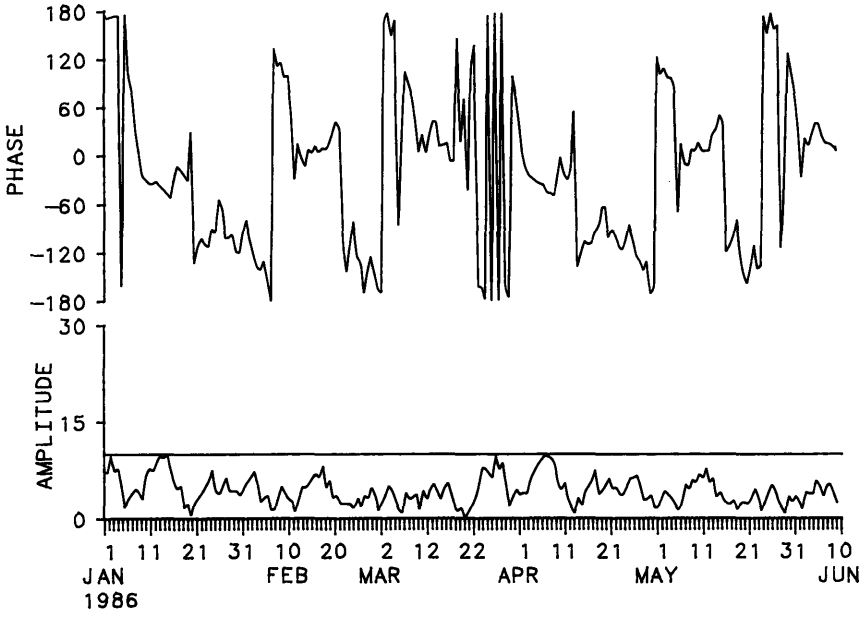

Figure 3.3: Results of a complex demodulation at the frequency f = 0.054 cph ($9.5 \times 10^{-5} s^{-1}$) on a time series of random numbers with the same range of values as current data at N6(10). Units of the amplitude are [cm/s].

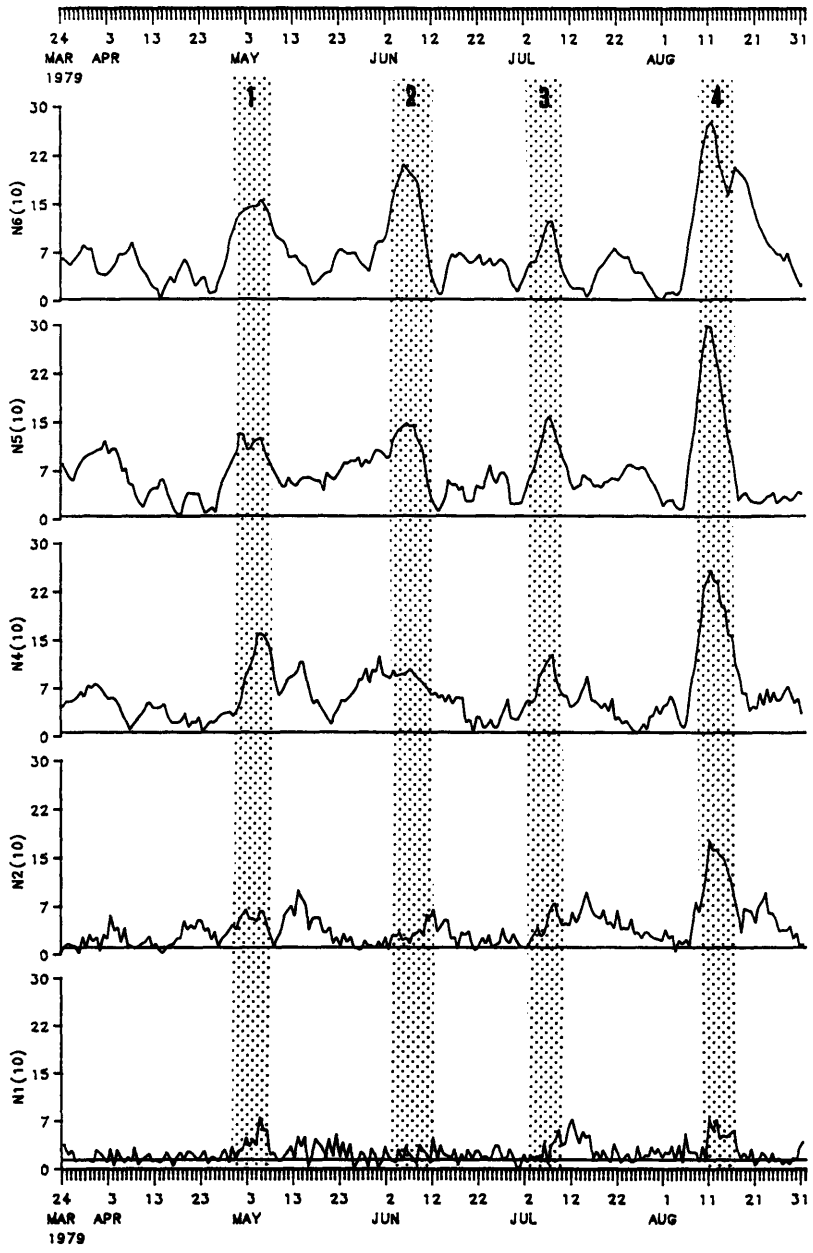

Figure 3.4: Time series of the amplitude (east component) of the complex demodulates at 10 m instruments, summer period. Units are [cm/s]. Stippled time periods mark the largest inertial events, which are numbered as in the text.

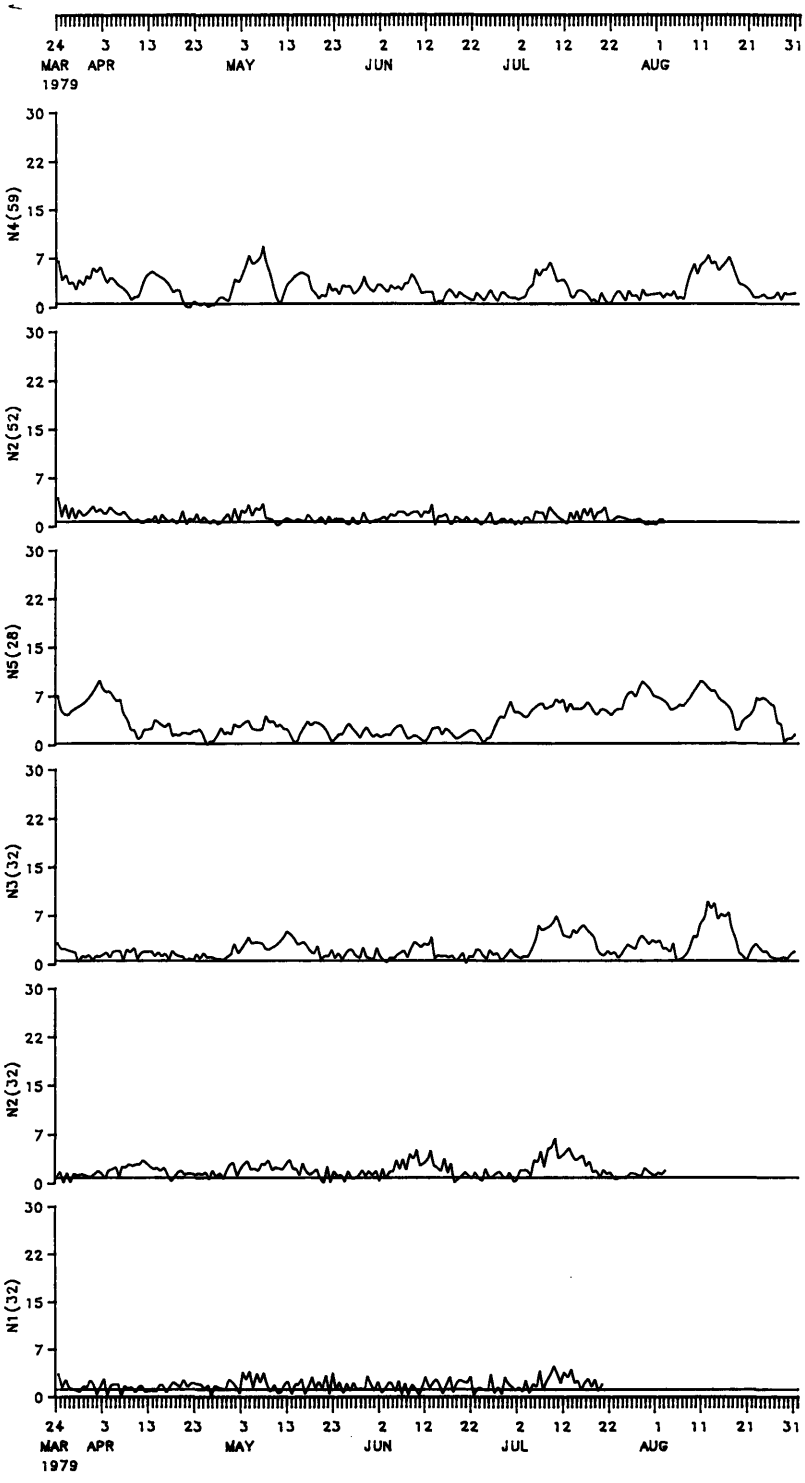

Figure 3.4 (continued): Time series of the amplitude (east component) of the complex demodulates at instruments deeper than 10 m, summer period. Units are [cm/s].

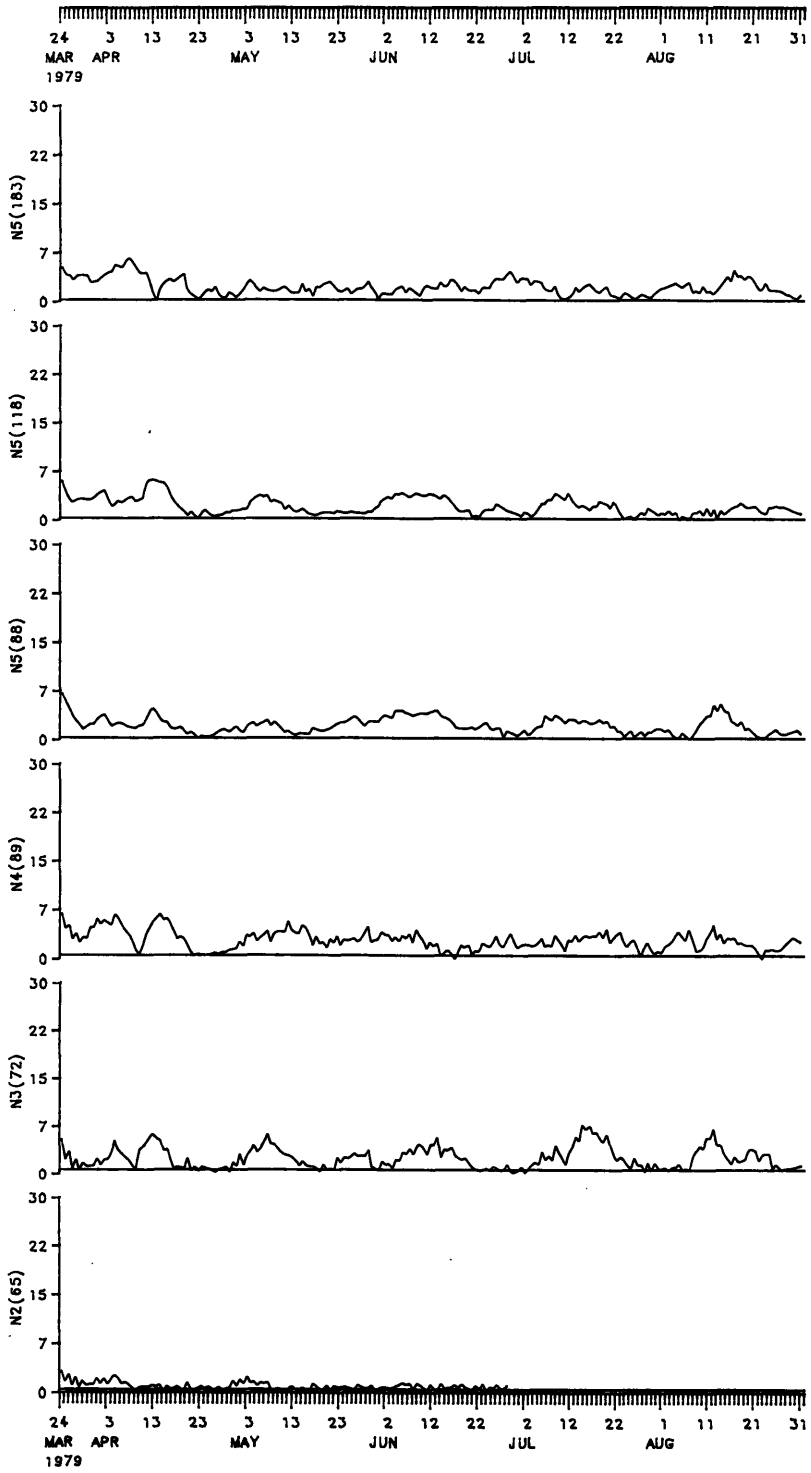

Figure 3.4 (continued)

from the tides. A more restrictive level was determined for N6(10) by demodulating a white noise signal. Rather than going through the same formal procedure at the other instruments, since the four events appear to be correlated at 10 m across the array, the amplitude was assumed to represent a real event at the other 10 m instruments when it stood out visibly against background levels. In addition, the events are visible in detided versions of the original current data at N4(10) and N5(10). In defining the duration of an event, it is helpful to consider the phase information as well as the amplitude information by taking the duration to be the period over which the rate of change of phase remains relatively constant. A line can then be drawn through the phase at each event from which a single value of ε, the deviation from the inertial frequency, can be estimated. These estimates are all within 3% of the demodulation frequency, satisfying the second criterion. Finally, although the figures are not shown, the east and north components of the velocity are nearly equal during these events at all of the instruments, with a phase difference of approximately 90°. Table 3.2 summarizes the characteristics of the events. N1(10) is not included in the table because, although there is a suggestion of higher amplitude around May 3, July 12, and August 12, the time series is too noisy and the phase behavior too erratic to make estimates of parameters.

Figure 3.5 is the same as Figure 3.4, but for the winter period. The most striking feature of the wintertime complex demodulates taken collectively is the universal drop in energy over the course of the winter period. The first few months are fairly energetic, at least at the 10 and 30 m instruments, but then the energy levels begin to decrease until they are very

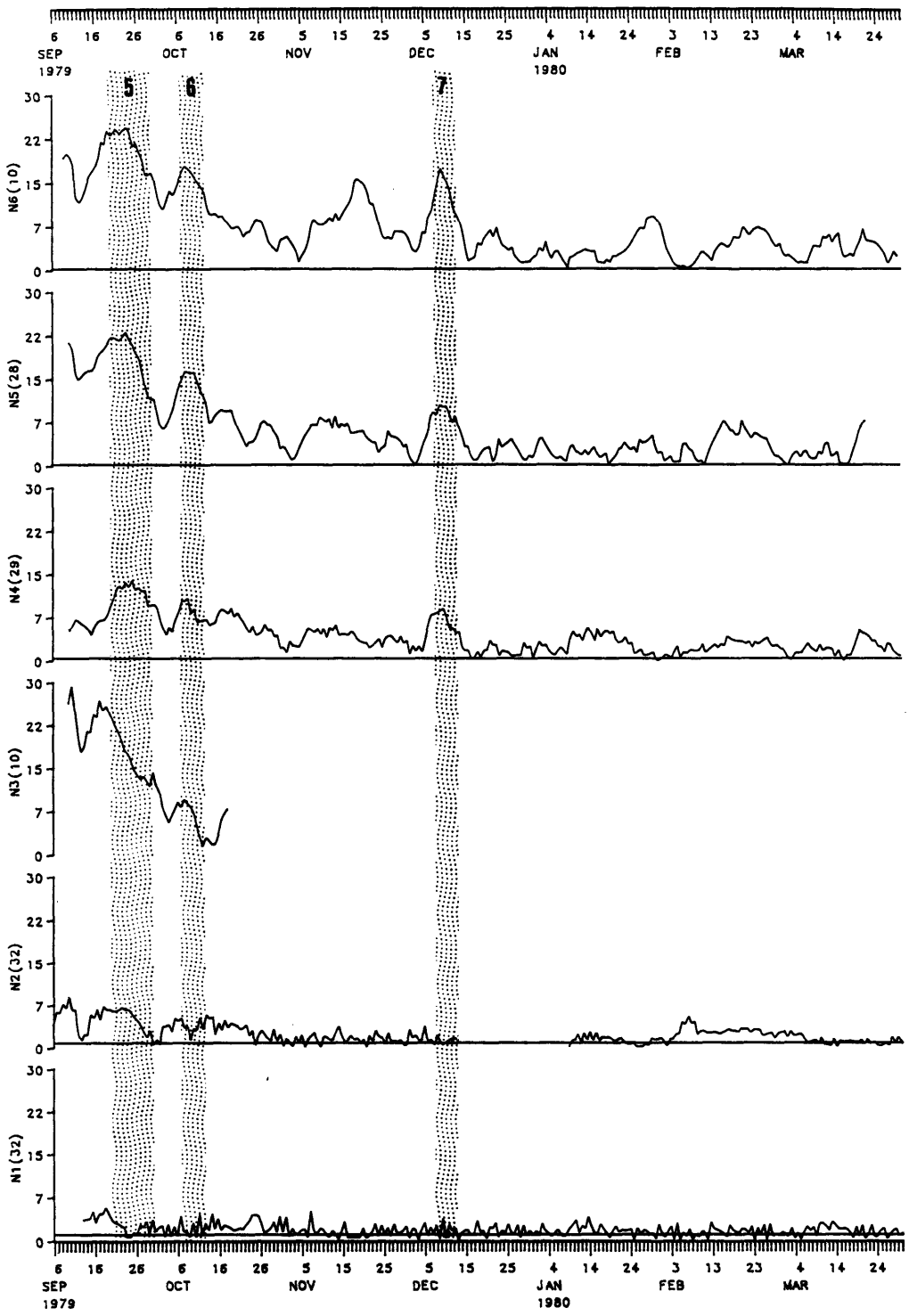

Figure 3.5: Time series of the amplitude (east component) of the complex demodulates at shallow instruments, winter period. Units are [cm/s]. Stippled time periods mark the largest inertial events, which are numbered as in the text.

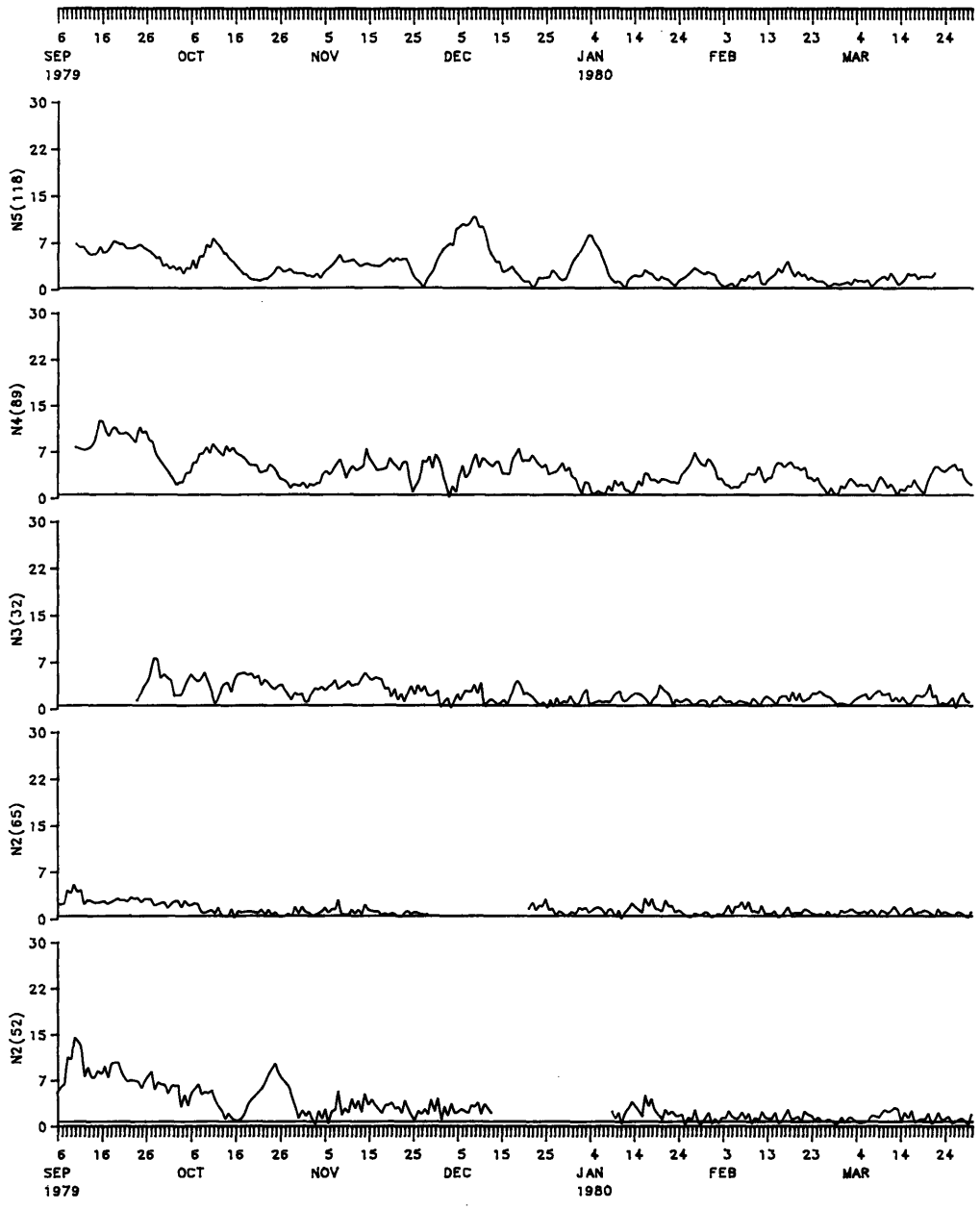

Figure 3.5 (continued): Time series of the amplitude (east component) of the complex demodulates at deep instruments, winter period. Units are [cm/s].

low everywhere by the beginning of 1980. Although the lack of data at 10 m is limiting, three events during the last four months of 1979 satisfy the criteria for a real inertial signal and appear to be coherent over instruments N6(10), N5(28) and N4(29); two of these are also seen in the short time series at N3(10). Table 3.3 summarizes the characteristics of these events. The first four months of 1980 are marked by low amplitudes at all instruments; there is almost no visual evidence of coherence except perhaps between N6(10) and N5(28) from the 15th to the 25th of February. A high amplitude event occurs at N5(118) centered on January 4, but there is no evidence of this event in the other time series.

The qualitative conclusions which follow from the complex demodulation analysis of the current meter data are:

1) High amplitude near-inertial events with time scales of O(10 days) are reasonably correlated at 10 m instruments at N4, N5 and N6.
2) Based on rough estimates of ε, most of the energy seems to be at subinertial frequencies.
3) At N2(10) the energy level is generally lower and not as highly correlated; i.e., the events dominating the time series at the other instruments cannot be unambiguously defined at N2(10), except for the 4th event.
4) The most energetic event (velocities 30 cm/s) centered around August 12 is clearly defined at all 10 m instruments seaward of mooring 1.

A complex demodulation analysis of the temperature data did not reveal any interesting features. This was as expected since there was no visual evidence of oscillations at the inertial frequency in the detided time series.

C. Horizontal Propagation Characteristics

Propagation horizontally across the array in an average sense is determined by the coherence and phase between pairs of instruments located at nearly the same depth on different moorings. This information is summarized for the summer and winter periods in Tables 3.4 and 3.5, respectively. None of the phase differences between horizontal pairs of instruments is significantly different from zero at 95% confidence. If, however, we ignore these error bars for the moment because they are based on a "worst case" situation in which the time series is actually white noise, a horizontal wavelength and phase speed can be calculated for each pair. A summary of these calculations is given in Table 3.6. The utility of these estimates is limited by (1) the scatter of the values, especially during the summer period, and (2) the unrealistic magnitudes of the values, also referring to the summer period in particular. Although the question of forcing has not yet been addressed, it will be shown that much of the energy in the inertial oscillations comes from the wind. The strongest inertial events can be associated with fronts which pass over the array at speeds of ~20 to 50 km/hr. The wavelength perpendicular to the front can be estimated as this translation speed times an inertial period, resulting in estimates from 370 to 930 km. At the outer shelf, horizontal wavelengths calculated from the coherence information clearly exceed the given upper bound. In addition no consistent estimate can be made because the values have such a wide range. During the winter the wavelengths are more reasonable, especially since fronts move with speeds closer to 50 km/hr during this time. However, the fronts generally propagate over the array in a southerly or southeasterly direction

which indicates that phase speeds would be directed offshore rather than onshore, contradicting the results in Table 3.6. Based on reasonable expectations for wavelengths and phase speeds, it appears that very little useful information about these quantities can be gained from the coherence and phase calculations.

The fact that the horizontal wavelength and phase speed estimates based on coherence/phase calculations are so inconclusive suggests that a spectral analysis technique, which averages the energy over the entire time series, is not the best way to investigate these quantities. The phase information from the complex demodulation can be used to look for propagation across the array on an event-by-event basis. A phase lag between the currents at horizontal pairs of instruments may represent propagation between the moorings; however, it is difficult to determine to what extent the phase lags are significant. One way of evaluating the stability of the phase estimates is to look at how they vary with the length of the segment used in the complex demodulation. In Figure 3.6, three different time series of the phase at N5(10) and N6(10), corresponding to three different piece lengths used in the complex demodulation, are plotted against a single time axis over the period of event 1. An analogous plot of the phases at N4(10) and N5(10) are shown on the second time axis. These plots show how the magnitude of the phase difference between the two instruments compares to the variance in the phase estimates at a single instrument when shorter segments are used in the complex demodulation. During event 1 the phase difference between the instruments remained relatively well-defined even when a piece length of ~3 inertial cycles was used. Figure 3.7 is a comparable plot

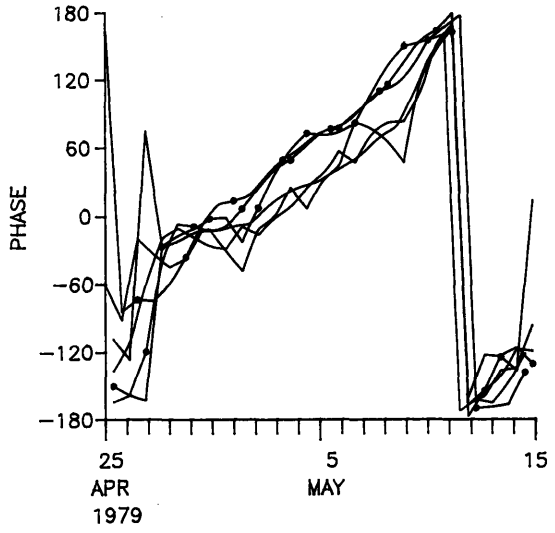

a.

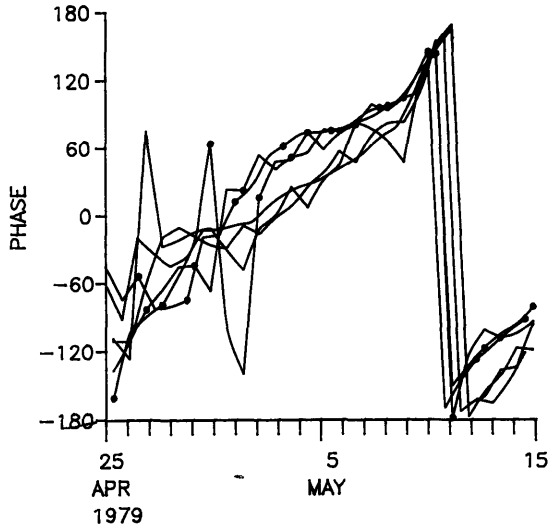

b.

Figure 3.6: Phase of the complex demodulate (east component) at (a) N5(10) and N6(10), and (b) N4(10) and N5(10) over the time period of event 1. N5(10) is denoted by the solid line (no symbols) in each case. The phase at each instrument is plotted three times, corresponding to three different piece lengths used in the complex demodulation. Piece lengths used were 180 hours (~10 inertial periods), 90 hours, and 54 hours. Note that the instrument at the lower phase leads that at the higher phase.

In this particular case, N5(10) appears to lead both N4(10) and N6(10), so that a consistent wavelength across N4, N5 and N6 can only be estimated if it is assumed that the wavelength is on the order of the mooring spacing (see Table 3.7).

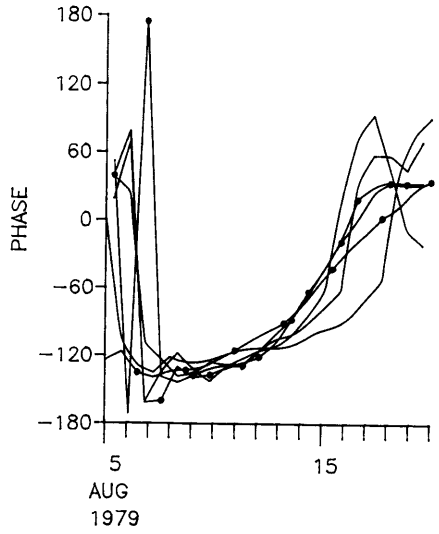

a.

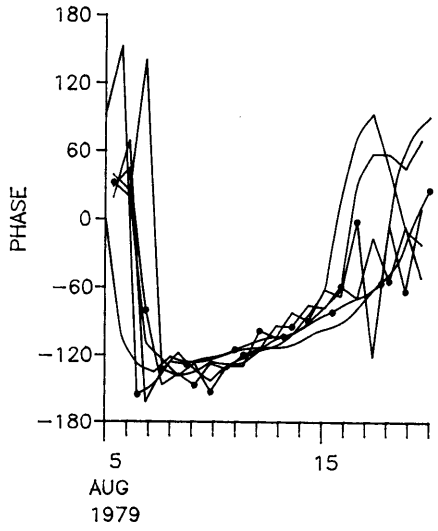

b.

Figure 3.7: Same as Figure 3.6, but for the time period of event 4.

for the time period covering event 4, over which the phase difference between the instruments is a small portion of the variance in the phase estimates for different values of the piece length. These two figures represent a "worst case" and "best case" over all the events and the reader can decide what significance to attach to these phase lags. No definitive statements about propagation and length scales can be made from such questionable statistics; nevertheless, in an attempt to obtain as much information as possible from the data, in the cases in which the phase lags were judged to be relatively stable to the piece length used, estimates of horizontal wavelength and phase speed were made from the phase difference between the moorings.

Even during the events for which meaningful estimates of the average phase lag can be made, there is an ambiguity. It may be assumed that (1) the horizontal wavelength is much greater than the mooring spacing, or (2) phase propagation is offshore and the horizontal wavelength is slightly greater than the mooring spacing when the seaward instrument appears to lead the shoreward instrument, and slightly less than the mooring spacing when the shoreward instrument leads the seaward instrument. Therefore, whenever the phase lag was judged to be stable enough to determine a reasonable value, wavelengths and phase speeds between moorings 4, 5 and 6 were estimated for the event using each assumption. If the horizontal wavelength is not aliased by the O(20 km) spacing of the moorings, then the phase lags over events 1-7 imply horizontal wavelengths λ_H ranging from about 200 to 500 km. This is high, but not completely unacceptable when compared to values calculated in previous work: Mayer et al. (1981) calculated a λ_H

of 280 km on the Middle Atlantic Bight, for example. Large horizontal wavelengths are for the most part associated with phase propagation onshore. N5 leads N4 during events 1 and 2, and N6 leads N5 during events 2 and 5, indicating onshore phase propagation. If, however, it is assumed that the horizontal wavelengths are undersampled by the mooring spacings (a direction of phase propagation must then be assumed), horizontal wavelengths of 19-23 km result, which is at the low end of previously observed values. Anderson et al. (1983) calculated a λ_H of O(20 km) off the Oregon coast. In order to do so they assumed that the wavelength was slightly less than the horizontal separation of the moorings, and that phase propagation was offshore.

The vertical structure will be shown below to resemble a first baroclinic mode. If the events are assumed to be freely-propagating normal modes then the dispersion relation could be used to dcetermine a reasonable horizontal wavelength. For the first baroclinic mode this relationship is

$$\lambda_H^2 = \frac{4N^2H^2}{\sigma^2 - f^2}$$

where H is the total water depth and σ is the frequency of the wave. Using $N^2 = 2 \times 10^{-4} s^{-2}$ and $H = 100$ m, a wave of frequency 1% above f requires $\lambda_H \gtrsim 200$ km; if $\sigma = 1.03\ f$ then $\lambda_H \gtrsim 100$ km. This calculation suggests that the larger wavelengths are more appropriate. There are inconsistencies, however: as noted in Figure 3.6, only a small wavelength gives consistent phase propagation across the array during event 1, and a large wavelength for event 5 requires phase propagation onshore, against the direction of propagation of the cold front associated with this event (see

Section III). Therefore, this does not constitute conclusive evidence that all the events are characterized by large horizontal wavelengths.

Attention has been focused on propagation along the array, but this does not exclude the possibility of propagation across the array. In the case of high-frequency internal waves, the direction of propagation is determined by the orientation of the major axis of the current ellipse. For near-inertial frequency waves, however, the current ellipse as calculated from the rotary spectra is so nearly circular that no useful information is gained by looking at the ellipse statistics (see Table 3.8). The ellipse stabilities are generally low and the orientation of the major axis is too variable to represent a meaningful average. In the absence of other information in the direction perpendicular to the array, it is difficult to say anything about the propagation of the near-inertial waves across the array.

D. Empirical Orthogonal Functions

A concise picture of the near-inertial energy across the array can be formed using empirical orthogonal functions, or EOFs. The analysis procedure is discussed elsewhere (e.g. Gonella, 1972; Kundu and Allen, 1976) and, in particular, rotary EOFs (Denbo and Allen, 1984) are used here since the clockwise rotating energy is specifically of interest.

The EOFs are "statistical modes" in which the data, or the Fourier transform of the data as in this case, can be expanded. They are the solutions to the eigenvalue problem

$$\sum_{i=1}^{K} C(x_i,x_j)\phi_m(x_i) = \lambda_m\phi_m(x_j),\ j=1,K\ , \tag{3.7}$$

where K is the number of positions, x_i is the position vector, and C is the rotary cross-spectral matrix over the inertial frequency band. C is defined by

$$C(x_i,x_j) = \sum_{k=f-(\Delta f/2)}^{f+(\Delta f/2)} [u_k(x_i) - iv_k(x_i)][u_k(x_j) + iv_k(x_j)],$$

where u_k and v_k are the Fourier coefficients of east and north velocities respectively at frequency k, and Δf is the bandwidth. If one mode is found to contain most of the variance then it is a concise representation of the relative magnitudes and phases of the current vectors rotating clockwise at near-inertial frequency at each instrument.

The largest EOF, which explains 69% of the variance during the summer period, is shown in Figure 3.8. The most striking feature of the EOF is the "modal" character of the response. If the motions represented waves propagating down from the surface, the eigenvector would turn at a more-or-less constant rate with depth. Instead, the deeper oscillations are nearly 180 degrees out of phase with those at the 10 m instruments, as would be expected if a first baroclinic mode is dominant. N3(32) and N5(28) current meters do not contribute significantly to the mode, perhaps because they are located near a node which could move up and down with ambient conditions such as mixed layer depth. Current meters N1(10), N4(89), N5(118) and N5(183) also do not contribute significantly; reference to Figure 3.2 confirms that this is as expected since these time series are not dominated by the same four events that dominate the others.

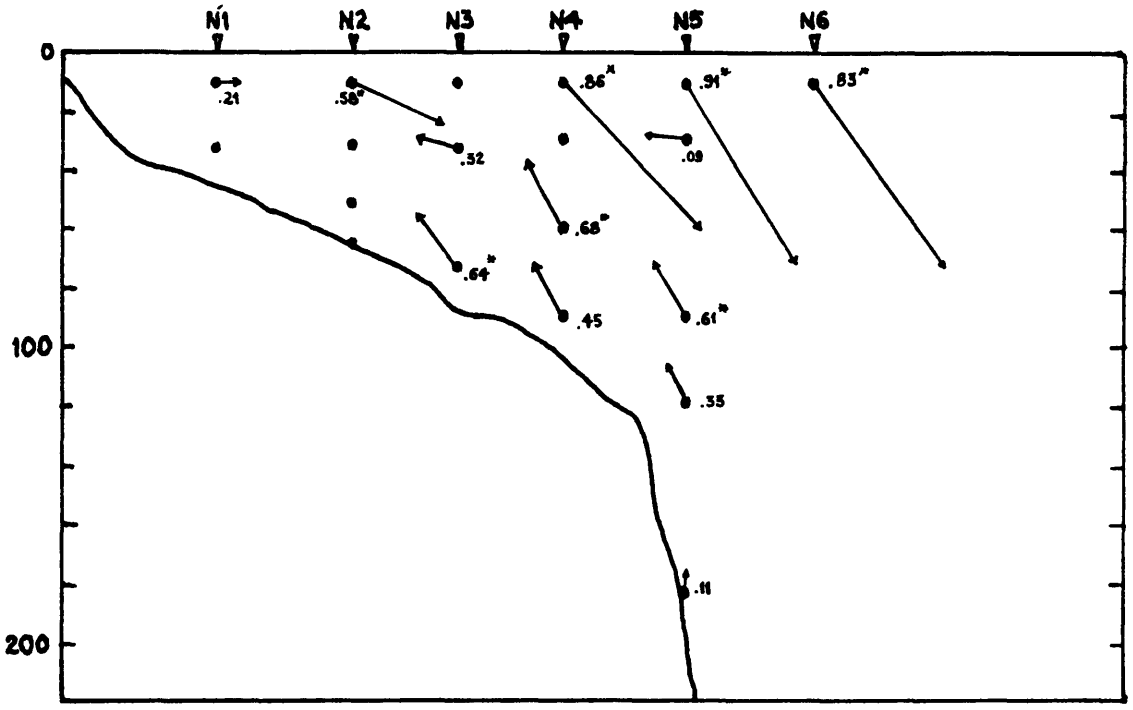

Figure 3.8: Eigenvector of the largest frequency-domain EOF for the summer period. The record used is from March 21, 1979 to September 5, 1979. The eigenvector has been normalized such that $\sum_{i=1}^{K} \phi_m(x_i)^2 = 1$. The phase is relative to an arbitrary zero value at N1(10). Coherence between the time series and the mode is given below the instrument label; values significant at 95% are denoted by (*). Normalized eigenvalue = .69.

Time series at N2 were omitted because they were much shorter and their inclusion requires elimination of events 3 and 4 from the calculation of the function. As a check on the "robustness" of the function, the calculation was repeated including the shorter time series. The percentage of the variance explained by the largest EOF is increased slightly to 72%. These results are shown in Figure 3.9. The modal character of the response is still dominant, the 10 m current meters at each mooring being nearly 180 degrees out of phase with the deeper current meters which contribute significantly to the EOF.

The variance in the second largest EOF is not insignificant. The second EOF explains 10% of the variance if the shorter time series are used and 16% of the variance if the longer time series are used. However, in both cases the second EOF picks out significant energy only at N5(28) which contributes very little to the largest EOF, and therefore they are not of interest here.

The wintertime EOFs contain fewer time series but some interesting comparisons can still be made. Figure 3.10 shows that the instruments N3(32), N4(29), and N5(28) are all highly coherent with the largest EOF and move nearly in phase with N6(10), suggesting that the surface layer has deepened. The upper (including 30 m) and lower velocities are still approximately 180 degrees out of phase, but the surface intensification is not nearly as strong as in the summer period. The instruments at N2 were not included because of the break in the time series there; however, for the time period August 7 to December 2, a coherence and phase calculation between the three instruments at N2 shows that N2(32) is coherent with

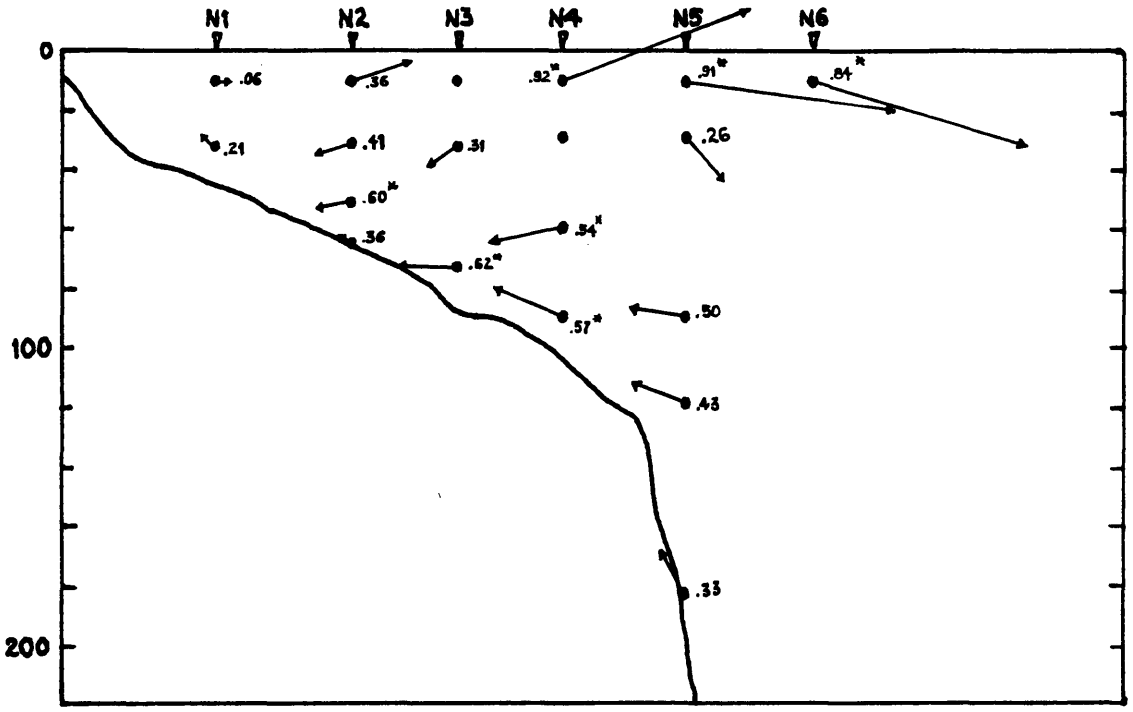

Figure 3.9: Same as Figure 3.8, with record from March 21, 1979, to July 2, 1979. Normalized eigenvalue = .72.

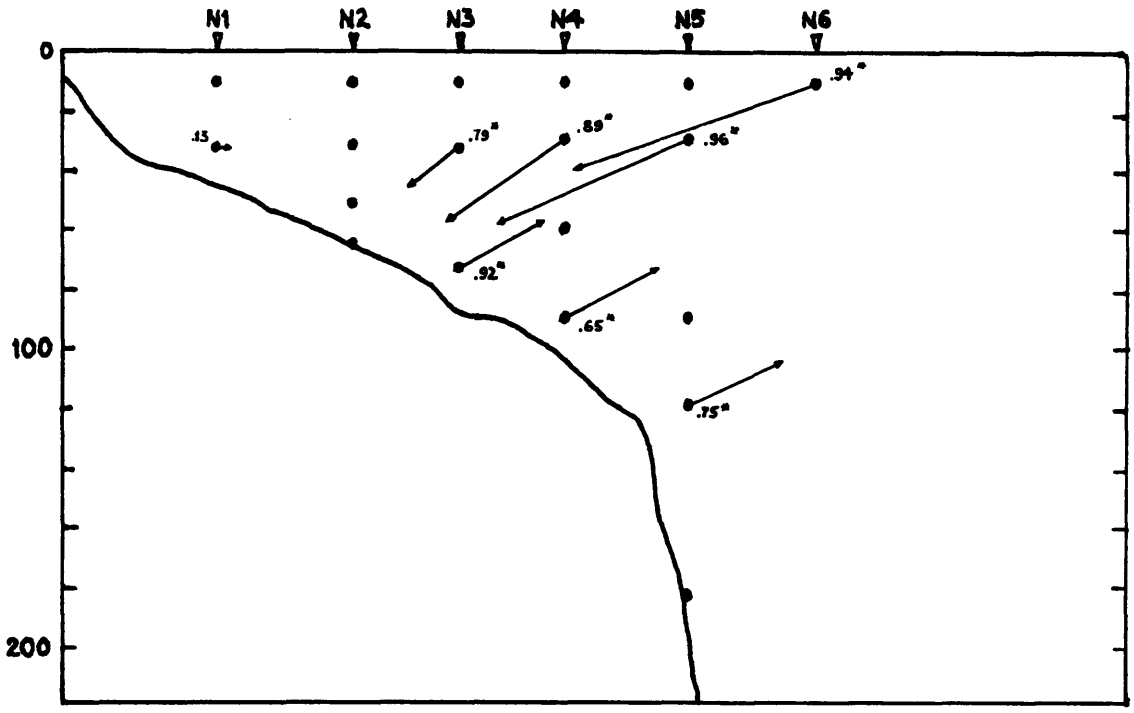

Figure 3.10: Same as Figure 3.8, for the winter period. Record used is September 2, 1979 to March 26, 1980. Normalized eigenvalue = .89.

N2(65) and leads by 0±43°, and N2(52) is coherent with N2(65) and lags by 8±11°. The coherence information suggests that the two-layer structure does not extend toward the coast as far as N2 during the winter.

Frequency domain EOFs are useful in determining phase relationships across the array but it is difficult to obtain information about temporal variation from these functions. It is impossible to be sure, for example, if the structure of the response in Figures 3.8-10 is present during all periods of high inertial energy or if it varies from event to event. A method for determining the temporal variability of the dominant mode of response is to solve for the time domain EOFs using the time series of the complex demodulates. The eigenvalue problem is

$$\sum_{i=1}^{K} R(x_i,x_j)\phi_n(x_i) = \lambda_n\phi_n(x_j),\ j=1,K\ , \tag{3.9}$$

where R is the covariance matrix of the time series of complex demodulates:

$$R(x_i,x_j) = \frac{1}{N}\sum_{k=1}^{N} v(x_i,t_k)v(x_j,t_k)\ ,$$

where N is the number of points in the series, and $v(x_i,t_k)$ is the amplitude of the demeaned complex demodulate at position x_i and time t_k. The eigenvector of mode n is ϕ_n and the eigenvalue is λ_n.

In this case, since the spatial structure of the inertial energy is known to be highly surface-intensified, the covariance matrix was normalized by the product of the standard deviations of the two time series, i.e.

$$R'(x_i,x_j) = \frac{1}{N}\sum_{k=1}^{N} \frac{v(x_i,t_k)v(x_j,t_k)}{\sigma_i\sigma_j} \quad ,$$

where

$$\sigma_i = \frac{1}{N}\left\{ \sum_{n=1}^{N} (v_i - \underline{v}_i)^2 \right\}^{1/2}$$

and $\underline{v}_i$ is the mean of the time series. This procedure renders the magnitudes of the eigenvectors difficult to interpret, but it prevents the mode from being dominated by the high variances at the energetic 10 m instruments. A time series of the amplitude of the first mode can then be constructed from the sum

$$A(t_k) = \sum_{i=1}^{N} \phi(x_i)v(x_i,t_k).$$

Figure 3.11 shows this time series calculated from the summertime complex demodulates. The first mode explains only 41% of the variance, but it is remarkably accurate in reproducing the major features of the complex demodulates; all four of the events from Table 3.2 are clearly visible. Twelve time series went into the calculation of the mode, and seven of these contribute significantly: N3(32), N3(72), N4(10), N4(59), N5(10), N5(88) and N6(10). Significant correlation was determined from an autocorrelation of each individual time series by taking the first zero crossing to be twice the decorrelation time scale. This probably results in an underestimate of the level of significance, since the true number of degrees of freedom will be greater than that assumed by this method because the time series are not

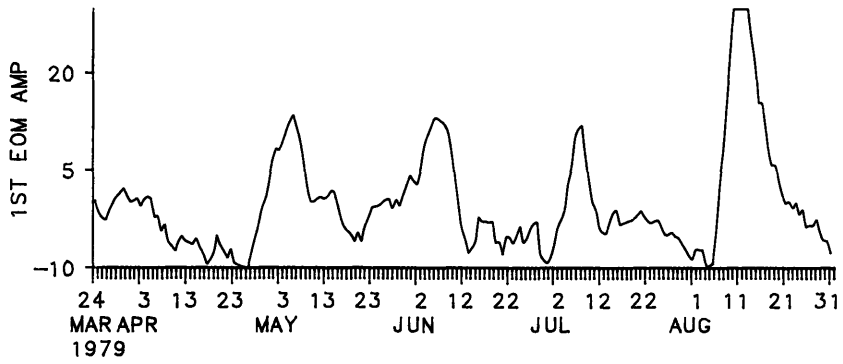

Figure 3.11: Time series of the amplitude of the largest time-domain EOF, summer period. The record used is from March 24, 1979 to August 31, 1979. Units are [cm/s], but the amplitude is offset by a mean value because all of the time series were demeaned. Normalized eigenvalue = .41.

perfectly correlated (Chelton, 1983). The result is quite satisfying because all of the time series which were coherent with the frequency EOF (except for N2(10)) are also correlated significantly with the time-domain EOF, leading to the conclusion that nearly all of the energetic inertial events are characterized by a surface-intensified vertical structure similar to that of the largest frequency-domain EOF. The time-domain EOF contains no phase information, but the phase information from the complex demodulation shows that the upper and lower layer velocities are 180° out of phase during the events, as seen in the frequency-domain EOF. The second largest EOF has a normalized eigenvalue of 0.18, almost half that of the first, but is only correlated with N5(28). Results for the wintertime are similar (see Figure 3.12). The largest EOF explains 56% of the variance. Eight time series were included in the calculation; N3(32), N3(72), N4(29), N4(89), N5(28) and N6(10) are significantly correlated with the mode. The second largest EOF has a normalized eigenvalue of 0.11, and is only correlated with N1(32). Again the largest EOF reproduces all of the major features of the complex demodulates and is significantly correlated with all but one (N5(118)) of the instruments that contributed to the frequency-domain EOF.

E. Summary

In the introduction it was indicated that there are three questions which could be addressed using the Nantucket Shoals data set. The first concerned the horizontal wavelength of inertial oscillations in the Middle Atlantic Bight. This question cannot be unambiguously answered, since a smaller horizontal mooring spacing is required to resolve the high wavenumber end of the range of possible values. The dispersion relation for

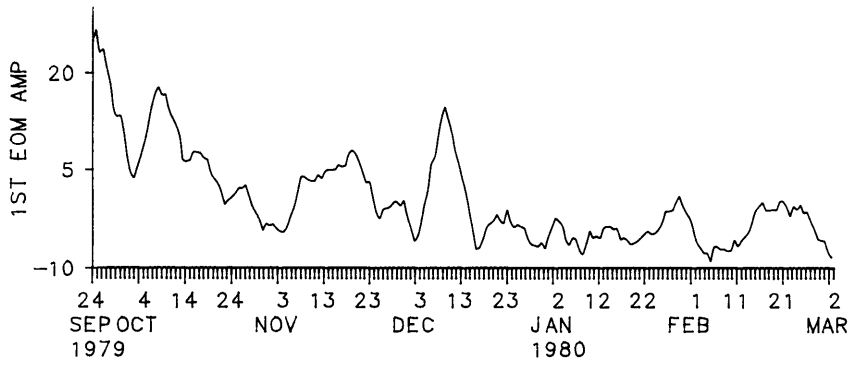

Figure 3.12: Same as Figure 3.10, for the winter period. Record used is from September 24, 1979 to March 22, 1980. Normalized eigenvalue = .56.

freely-propagating waves suggests that wavelengths O(100 km) are reasonable, but this is not completely satisfactory. Discussion of the generation of the oscillations in the next section indicates that offshore phase propagation is expected for most events; phase information from a complex demodulation of the time series shows that large-scale disturbances as predicted by the dispersion relation could be propagating offshore during events 3, 4, 6 or 7 but not during events 2 and 5. In addition, consistent propagation during event 1 is only possible if it is assumed that the horizontal wavelength is small, O(20 km).

The second question concerned the vertical structure of the near-inertial motions. This structure is concisely represented by the largest EOF which has the appearance of a first baroclinic mode. The upper layer is deeper in the winter than in summer, consistent with the deeper mixed layer during the winter period. This vertical structure is not uniform across the shelf; rather, it is characterized by a decrease in energy toward the coast and appears to extend as far as N2 during the summer but only as far as N3 during the winter. The horizontal variation is probably due to the effects of the coast and the shoaling topography and the seasonal variation reflects changes in the stratification. These are features which will be touched upon in the next section.

In response to the last question posed in the introduction, there is little evidence that the deep ocean is exerting a strong influence on the near-inertial wave field over the shelf. The EOF analysis shows a gradual decline in inertial energy toward the coast, but no dramatic concentration of inertial energy near N5 or N6 as might be expected if the deep ocean were

an important source. The direction of propagation across the shelf break has not been established, nor is it clear that there is such propagation. However, if one examines the data on an event-by-event basis, Figure 3.4 shows that event 2 is characterized by a much more rapid decay in energy away from the shelf break than the other events. This event will be discussed in some detail in the next section, and it will be argued that the energy did, in fact, originate in the deep ocean south of the array.

IV. Discussion

The discussion is organized into four parts. In the first part, local forcing by the wind is considered. As a first attempt at associating events in inertial energy with local winds, the momentum equations are reduced to a balance between forcing by the wind stress at the surface, linear damping, and the time derivative and coriolis acceleration of the currents. These equations can then be integrated forward in time using the observed wind data. The momentum equations in this form act as a very crude filter which picks out those times when the wind stress is changing in such a way as to generate inertial oscillations efficiently. Because the momentum equations are reduced to unrealistically simple physics, only the gross features of the inertial currents can be reproduced, even if wind forcing is dominant. However, the use of these equations with the observed winds is a worthwhile exercise, since it offers a straightforward way to see whether wind forcing can account for observed maxima in the inertial energy.

In the second part the discussion turns to how the vertical structure is generated in response to forcing at the surface, and what this structure is expected to look like. The vertical structure cannot appear until there is horizontal convergence in the mixed layer. Because horizontal convergence can occur in two different ways over the shelf (either through horizontal variation in the wind stress or the presence of the coastal wall), two simple cases are considered, demonstrating the two mechanisms separately. In the first case an initial distribution of horizontally varying currents (which could equivalently be a horizontally varying wind stress) produces a

response which should be dominated by the first baroclinic mode for all times of interest. In the second case a horizontally uniform wind with a delta function time dependence is used to force an ocean in the presence of a coastal wall. For distances sufficiently far from the coastal wall this solution will also resemble a first baroclinic mode. With the given data set, it does not seem possible to distinguish between the two mechanisms, both of which explain the vertical structure of the observed currents.

Finally, two aspects of the shelf environment which may significantly influence the inertial wave field are considered: the mean geostrophic flow and the sloping bottom topography. It is suggested that the mean flow can alter the observed frequency of the near-inertial waves and can cause the transfer of inertial energy from large to small scales. The expected changes in flat-bottom results due to the presence of a bottom slope are also discussed, but there is little evidence of these changes in the data.

A. Local Forcing

The surface intensification of the inertial currents suggests that they are forced at the surface by the local winds. This conclusion is supported by weather maps covering the time period of the experiment; examples of these are shown in Figure 4.1. Most of the energetic events described in the last section can be associated with a front passing over or near the array.

Generation of inertial oscillations by the wind is not governed by a simple proportionality between the strength of the wind and the magnitude of the inertial currents. A constant wind, for example, generates increasing

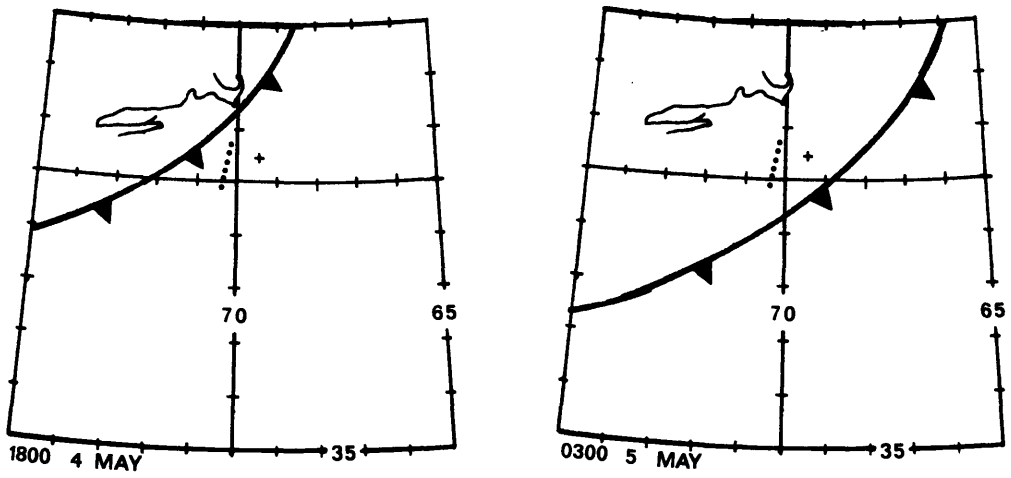

a.

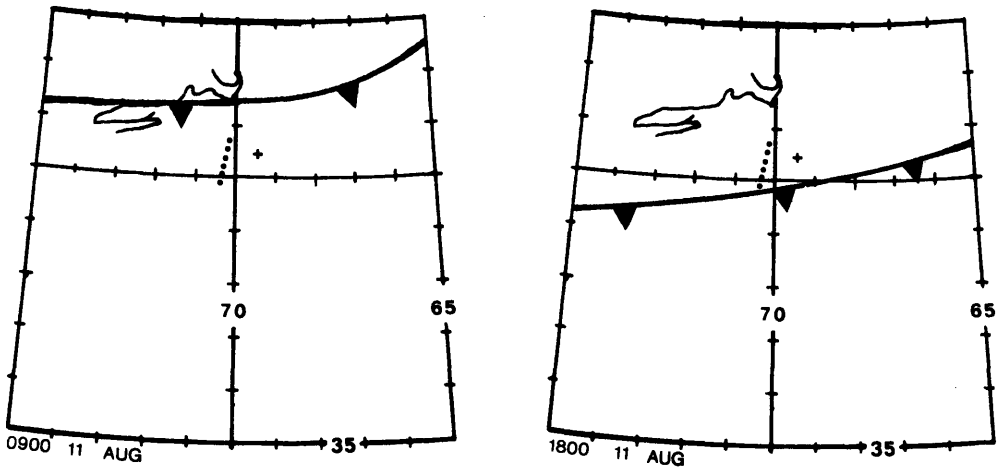

b.

Figure 4.1: Adaptations of National Weather Service maps showing examples of atmospheric disturbances associated with events. Dots represent approximate positions of the moorings, "+" represents NLS buoy, and heavy lines indicate approximate positions of the fronts. (a) event 1, (b) event 4.

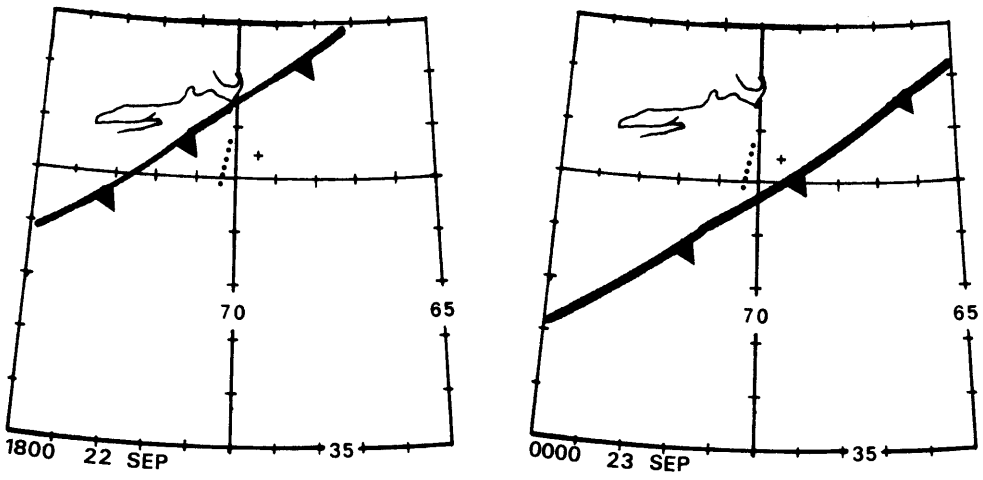

a.

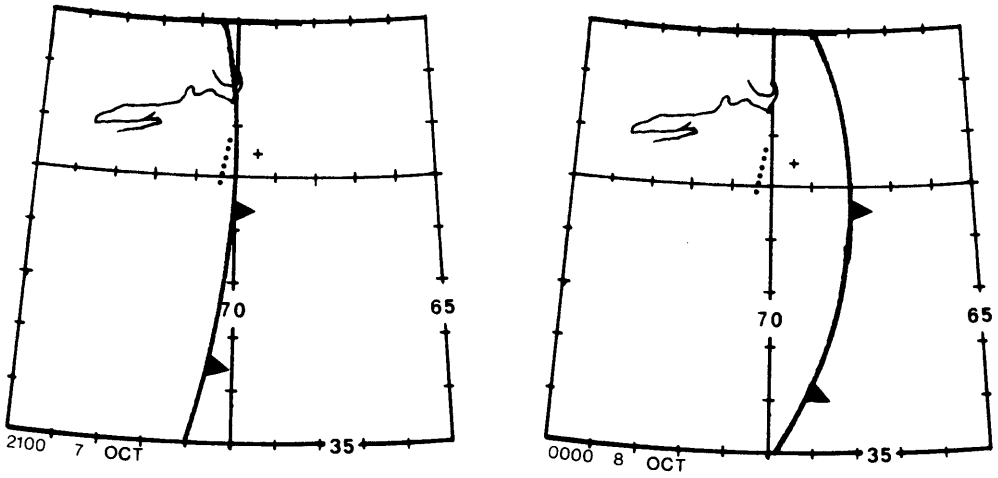

b.

Figure 4.1 (continued): (c) event 5, (d) event 6.

inertial currents for a time up to half an inertial period, but after this time the same wind will begin to extract energy from the inertial currents. If a constant wind blows for an entire inertial period it will have removed all of the inertial energy during the second half of the period that was put in during the first half of the period (Gill, 1982, pg. 323). A rapid change in the direction of the wind, even if its magnitude is not great, has the potential to generate large inertial currents if the currents generated by the rotated wind vector are in phase with the previously existing currents. Similarly, a rapid change in direction can destroy inertial oscillations if the new currents are out of phase with the previously existing currents.

The basic physics necessary for the exchange of energy between the wind and the inertial currents were included in a very simple model of a slab-like mixed layer by Pollard and Millard (1970, hereafter PM). The equations governing the motion in the mixed layer are

$$u_t - fv = \tau^x/\rho h - cu, \tag{4.1.a}$$

$$v_t + fu = \tau^y/\rho h - cv, \tag{4.1.b}$$

where u and v are the depth-averaged velocities in the x and y directions, respectively, ρ is the density in the mixed layer of depth h, and f is the local Coriolis parameter. The drag coefficient c is intended to model the drain of energy due to the radiation of waves away from the base of the mixed layer, and τ^x and τ^y are surface stresses. The free solutions to (4.1) are damped inertial oscillations

$$u = ae^{-ct}\sin(ft) - be^{-ct}\cos(ft)$$

$$v = ae^{-ct}\cos(ft) + be^{-ct}\sin(ft)$$

and the forced solution will also contain an aperiodic Ekman transport. These equations can be integrated forward in time, generating a time series of the velocity in a mixed layer of depth h in which the balance is between surface forcing by observed winds, the acceleration of the fluid, and damping by wave radiation. PM noted that the agreement between the currents generated by the model and inertial currents at site D (39°10'N, 70°W) was at times quite good. Several other authors have used this highly simplistic model (e.g. Kundu, 1976; Anderson et al., 1983) with some success. In general, their findings indicate that the PM model reproduces some gross features in the inertial energy quite well, although there are always occurrences of high-amplitude inertial oscillations which are not accounted for.

The PM model was used to generate mixed layer velocities during the period covering each of events 1 through 7 which were defined in section III. The wind stress data used were calculated from the Nantucket Light Ship wind measurements as described in section I. The mixed layer depth was estimated from hydrographic sections dated as closely as possible to the event, with the exception of event 1. In this case a mixed layer depth of 10 m gave reasonable amplitude agreement even though it appears anomalously shallow for this period. In general, the mixed layer depths estimated from the hydrographic sections are subject to much uncertainty, but this was considered preferable to assuming a single value since the stratification does change substantially from event to event. This can be seen in Figure 4.2 which shows hydrographic sections taken throughout the year-long experiment.

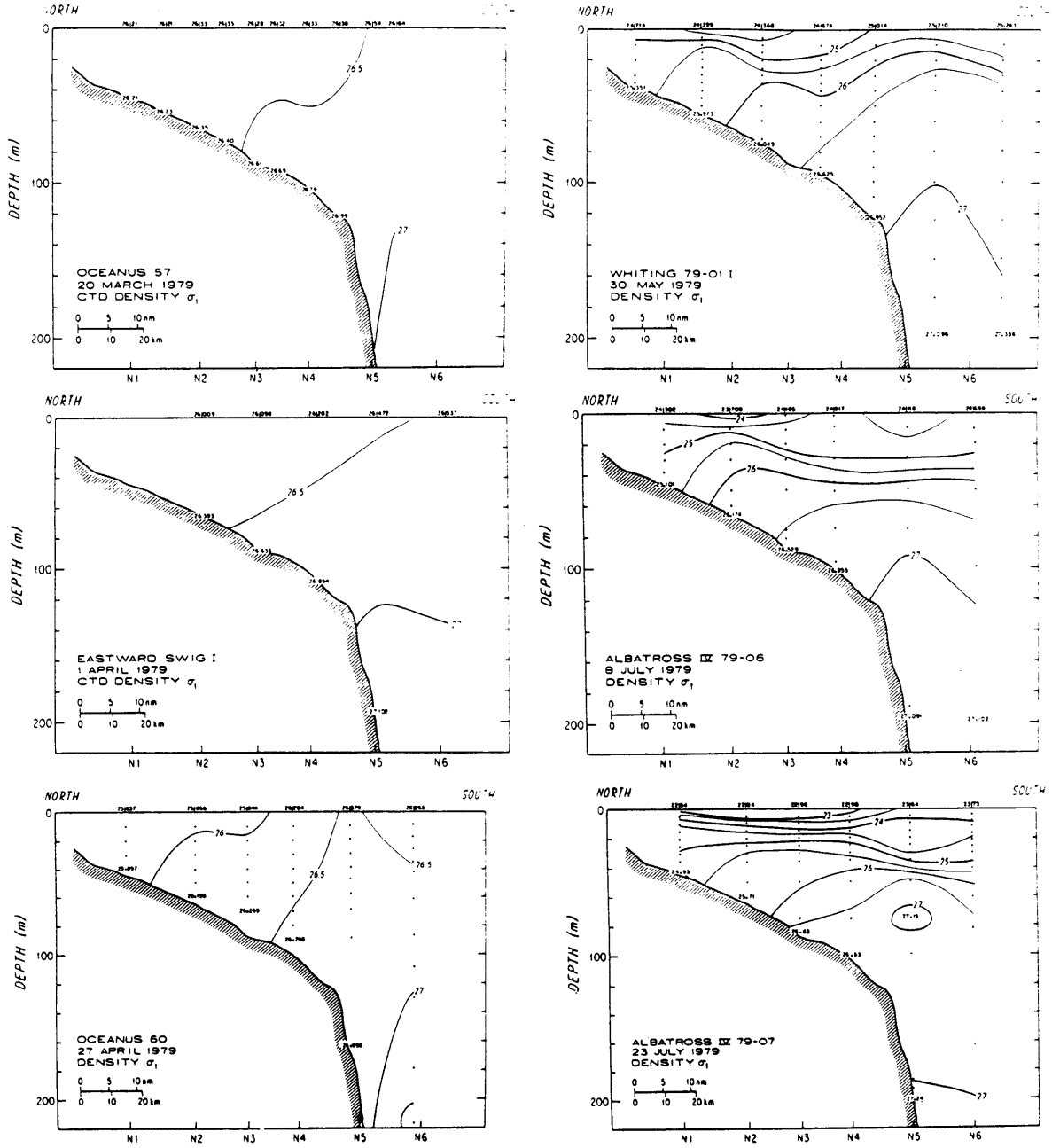

Figure 4.2: Density (σ_t) sections obtained along the NSFE mooring transect, from Wright (1983).

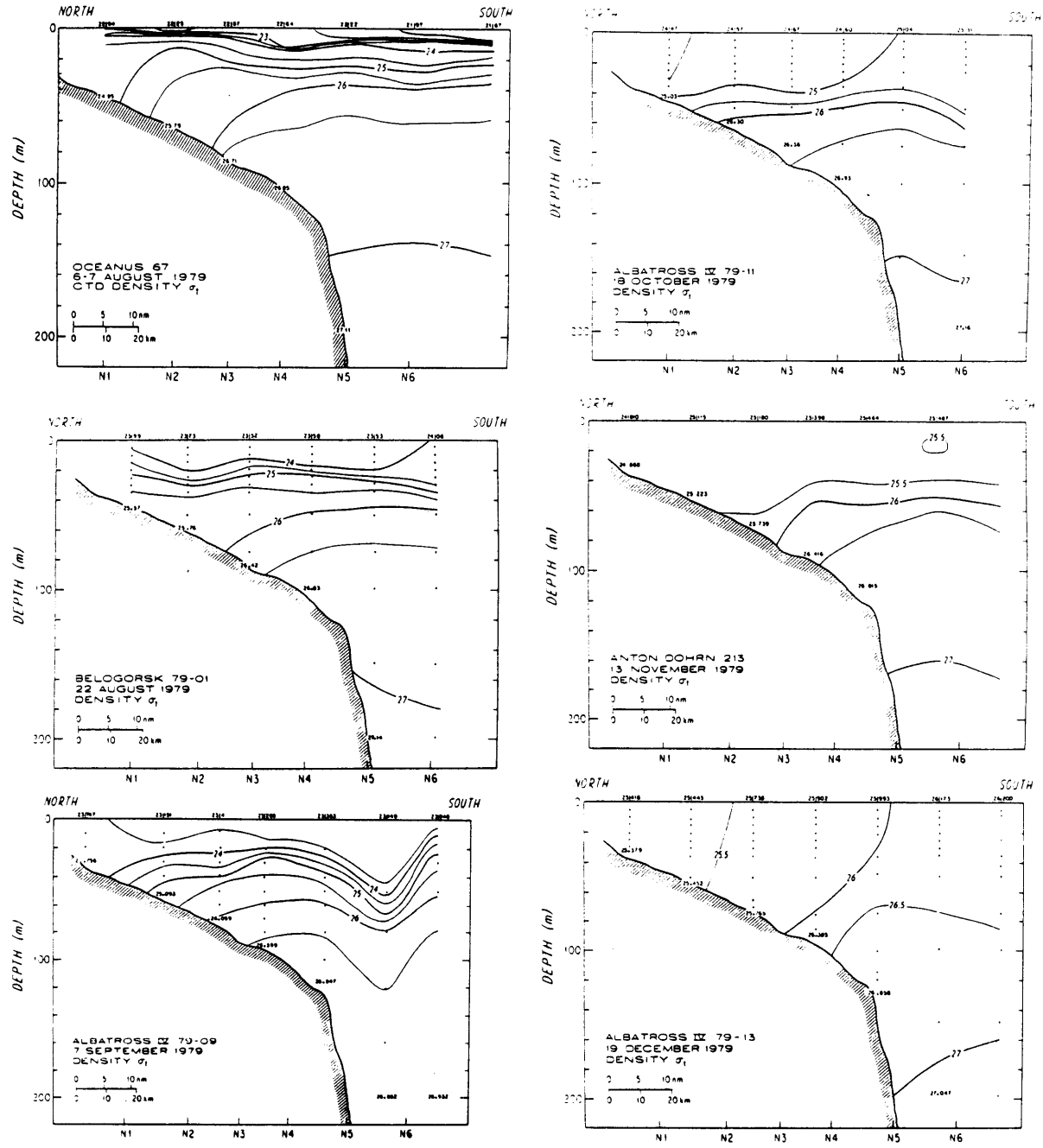

Figure 4.2 (continued)

The water column is nearly homogeneous during the first few months until sometime in May, then the water column gradually becomes more stratified through the summer reaching maximum stratification (and minimum mixed layer depth) sometime in August. At this point the mixed layer begins to deepen and the water column becomes homogeneous again by the middle of December (see Beardsley et al., 1985, for more details).

The PM velocities were demodulated at a frequency of 0.054 cph as described in section 3. Figure 4.3 shows the amplitude and phase of the complex demodulate of the PM velocities and the currents at N4(10), N5(10), and N6(10) (summer) or N4(29), N5(28) and N6(10) (winter) over each event. A decay constant of $c = (5 \text{ days})^{-1}$ was chosen subjectively as a value which resulted in good overall agreement in event amplitudes while bringing background levels down to reasonable values at other times. All events except 2 are "reproduced" by the PM model, in the sense that a maximum in the PM currents corresponds to the occurrence of an event. The spin-up and decay of the modeled event often differ considerably from that of the observed event, and the time of maximum current may differ by several days. The phases are not, in general, in good agreement. However, it should be remembered that the PM equations are expected to predict only the crudest features of the inertial energy, and that good agreement in amplitude or phase would simply be fortuitous. The only conclusion to be taken from Figure 4.3 is that probably the local wind stress was an important factor in driving all of the events with the exception of 2, a conclusion which is supported by weather maps covering the time periods of the events. Note that this does not necessarily mean that 2 is <u>not</u> a wind-driven event, only that the PM model cannot confirm that it <u>is</u> a wind-driven event.

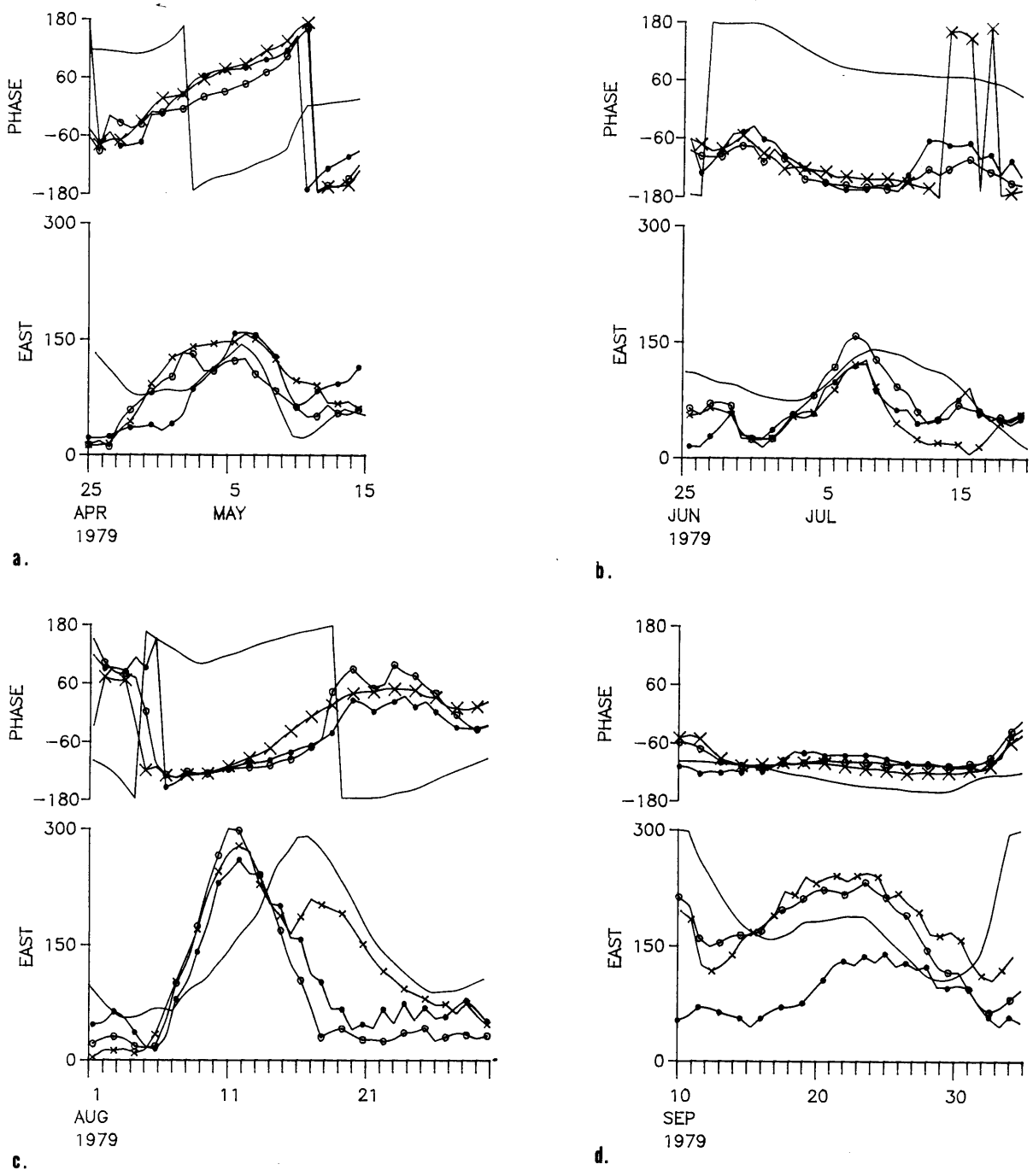

Figure 4.3: Magnitude and phase of complex demodulates, damping time scale = 5 days. Solid line (no marks) indicates currents obtained from Pollard and Millard model.
a) Event 1, h = 10 m. b) Event 2, h = 15 m
c) Event 3, h = 15 m d) Event 4, h = 10 m

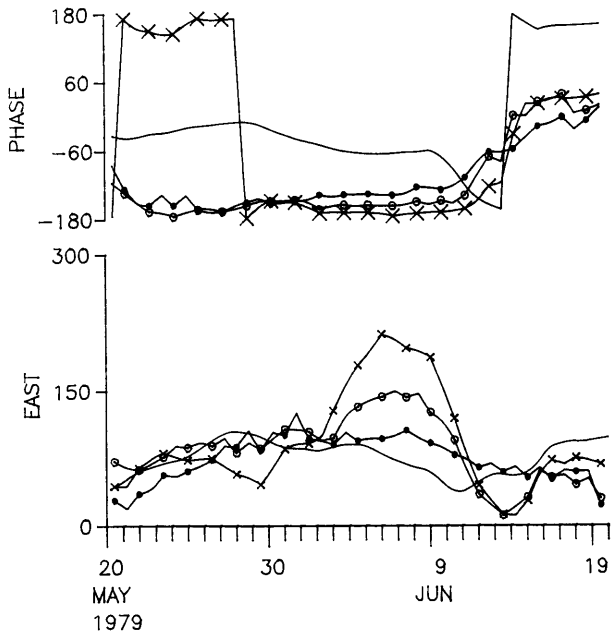

e

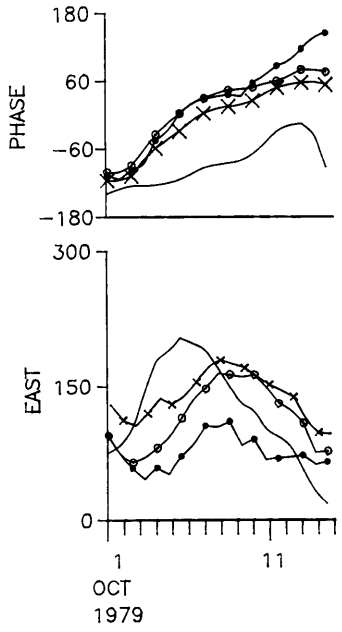

f.

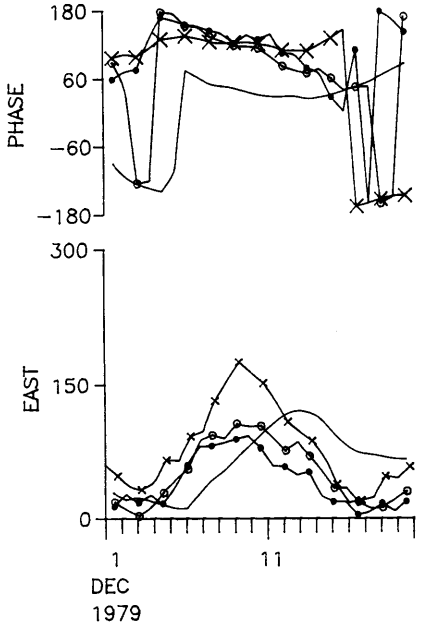

g.

•: N4(10)
o: N5(10)
x: N6(10)

Figure 4.3 (continued):
e) Event 5, h = 25 m
f) Event 6, h = 40 m
g) Event 7, h = 50 m

The Rayleigh friction is an ad hoc way of removing energy from the mixed layer and does not model the real physics involved; it is simply a parameter used to "tune" the model so that it gives the most realistic results. However, some statements about the characteristics of wind-driven inertial oscillations can be made by observing the effect of the choice of damping coefficient on the PM model. Figure 4.4 shows the results of changing this decay constant to $(6 \text{ days})^{-1}$ for the summer events. Event 2 is not included since it does not appear in the PM currents even when the parameter c is changed. The winter events are not included because the results are not noticeably different for $c = (6 \text{ days})^{-1}$. Notice first that the choice of a single value for all the events is not the best parameterization. Event 1, for example, is described better by a damping coefficient of $(5 \text{ days})^{-1}$ than $(6 \text{ days})^{-1}$, and vice versa for events 3 and 4. This apparent change in the appropriate "memory" for the model may be linked to differences in stratification or horizontal length scale which affect how fast energy can disperse out of the mixed layer. Since the greater stratification of the water column during events 3 and 4 would tend to increase the propagation of energy out of the mixed layer in the form of internal waves, the longer residence time of the energy in the mixed layer during these events may indicate that they are of larger horizontal scale than event 1. This conclusion follows from the fact that at near-inertial frequencies waves of large horizontal wavelength propagate energy vertically more slowly than waves of comparable vertical wavelength and small horizontal wavelength (see, e.g. Gill, 1982, ch. 8). This assumes that dispersion of energy out of the mixed layer is due primarily to the radiation of internal waves, an

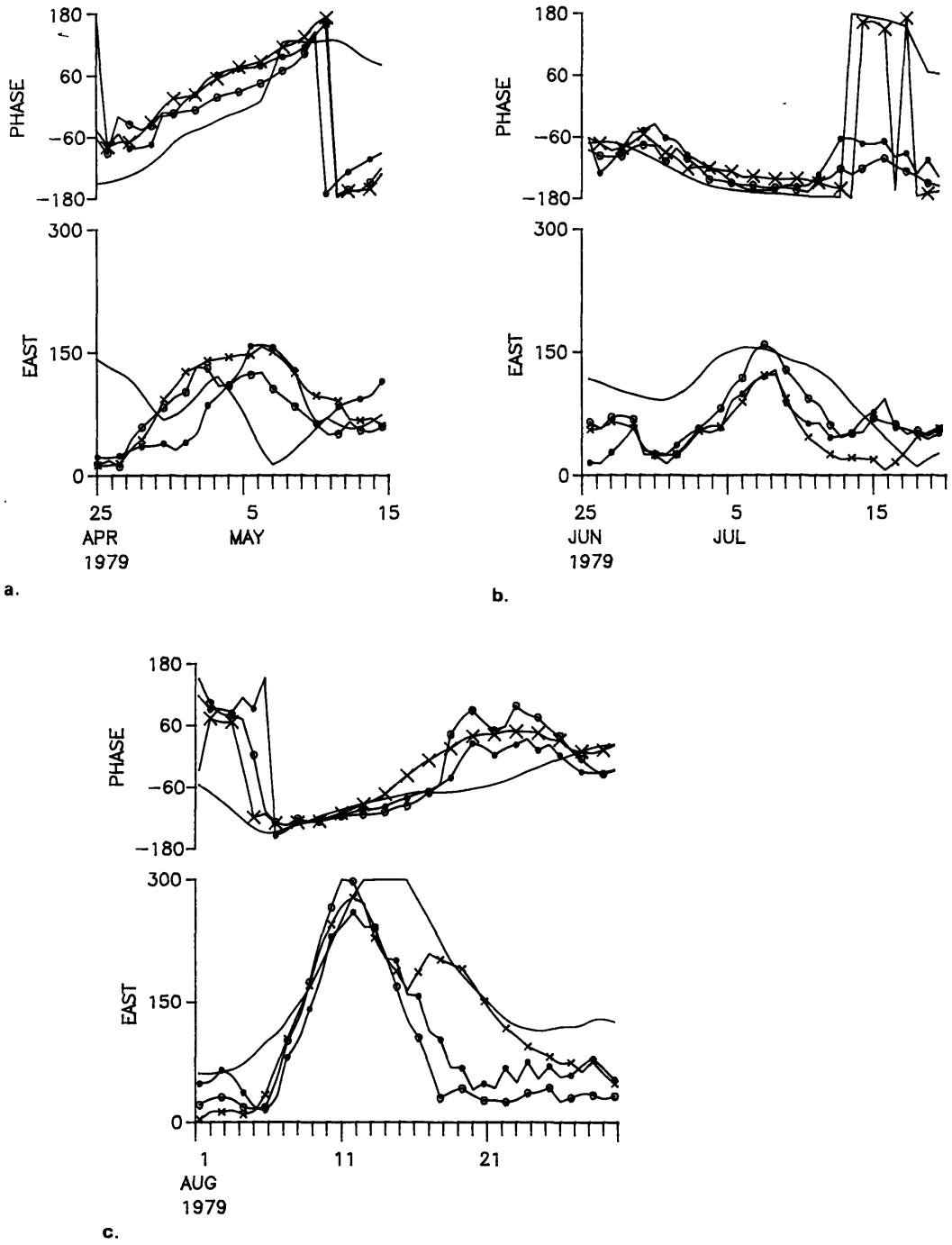

Figure 4.4: Magnitude and phase of complex demodulates, damping time scale = 6 days. Solid line (no marks) indicates currents obtained from Pollard and Millard model.
a) Event 1, h = 10 m
b) Event 3, h = 15 m
c) Event 4, h = 10 m

assumption which, it should be noted, is not necessarily justified. Second, a difference in the effect of the damping coefficient is seen between the summer and the winter months. Events 5, 6 and 7 (winter period) are relatively insensitive to the choice of the parameter c: a change of 3 days in the damping time scale produces a small change in amplitude and almost no change in phase (figures not shown). Since the winds during the winter period are much stronger than during the summer, the response to a wind event will be much less dependent on the initial conditions of the currents during the winter than during the summer. This can be understood if the response to a wind event is considered as a vector sum of an initial current and a new current forced by the change in the wind. This sum will be dominated by the new current if this current is strong, but if the two currents are of comparable magnitude, the initial conditions will be important in determining the sum. Since the damping coefficient largely determines the magnitude and phase of the mixed layer currents at the beginning of any inertial event, the response to the weak winds of the summer is expected to be more sensitive to the choice of this parameter. In addition, the average magnitude of the inertial currents is greater over the first part of the winter period so that the product "cu" is not as sensitive to the choice of c as it is when the average magnitude of the inertial currents is lower, as during the summer period.

A change in the nature of the damping coefficient occurs when the water column is homogeneous, i.e. the "mixed layer" extends to the bottom. The damping coefficient is no longer modelling the radiation of energy due to internal waves, but rather dissipation due to bottom friction. Figure 4.5

shows the time series of low-pass filtered wind stress over the period of the NSFE experiment. There is a period of high winds at the beginning of the experiment during March and April, then the winds die down and pick up again in October, after which they are strong during almost the entire winter period. If the damping coefficient is kept at $(5 \text{ days})^{-1}$ or $(6 \text{ days})^{-1}$, then the PM model predicts large mixed layer currents during the periods of strong winds, but the energy level of the inertial oscillations in the observed currents is low. Referring to Figure 4.2, it is clear that the strongest winds occur when the water column is nearly homogeneous, in which case the correct parameter to use becomes the bottom friction coefficient. If the PM model is run using an "interfacial stress" equal to r/h, where h is the depth of the water column (~100 m) and r is the bottom friction coefficient (~.1 cm/s), then the equivalent $c \approx (1 \text{ day})^{-1}$ and the energy at the inertial frequency is reduced to the noise level during the periods of high winds. Bottom friction strongly damps inertial motions, so that if the water column is well-mixed, even very strong winds cannot generate strong currents.

The PM model can be used to establish qualitatively that much of the inertial energy during NSFE originates in the wind at the surface, but it cannot begin to model the details of the time evolution of the inertial energy. However, because the model is so simple, it is easy to pinpoint some of the physics that should be added in order to model accurately the generation and decay of wind-driven oscillations in the mixed layer of the real ocean. Three primary deficiencies in the model point to the missing physics: (1) the model allows no horizontal variation and therefore no

horizontal propagation, (2) the mixed layer is modeled as a slab of constant thickness, and (3) there is no active layer beneath the mixed layer. Consideration of these deficiencies is worthwhile since it leads to some further insight into the more complicated processes actually taking place as the inertial oscillations grow and decay. The first two deficiencies are discussed briefly below. The consequence of having no active lower layer coupled to the mixed layer is that the bottom cannot influence the response and no vertical structure can be predicted. A discussion of the vertical structure predicted by very simple models that include an active lower layer is given in part (B) of this section.

The lack of horizontal variation or propagation is probably not important when the local winds are efficiently generating inertial energy. However, consider event 2, which does not appear in the PM currents. The amplitude of this event decreases monotonically from N6 and is reduced almost to the noise level at N4. Since this event does not exhibit the large coherence scale of the other events or of the winds and is largest at the shelf break, it is likely that the oscillations either originated at the shelf break, or originated offshore of the shelf break and propagated onto the outer shelf through the open boundary. Generation at the shelf break could occur through interaction of surface-generated inertial currents with the shelf break topography (Prinsenberg et al., 1974); however, then the event would be characterized by a concentration of energy in a beam closely paralleling the bottom, especially since the bottom slope on the shelf is close to the characteristic slope (see Appendix). The complex demodulation of the time series across the array (Figure 3.3) shows that this event is

surface-intensified; consequently, it probably began as a wind-driven disturbance incident on the open boundary at the shelf break. Existing theory predicts that a wave propagating up a slope would show a concentration of energy near the bottom (Wunsch, 1968, 1969); there are two reasons why this does not happen for event 2. First, since near-bottom velocities are small in this case, the event would not necessarily become bottom-intensified as it penetrated the shelf. Second, the event does not get far enough onto the shelf to be severely altered by the bottom slope. Since it would now be contradictory to argue that the bottom slope inhibits the propagation of the event, another explanation is required for the decay in amplitude from N6 to N4. This is easily found by remembering that the shelf south of Nantucket Shoals is oriented approximately east-west, therefore slightly superinertial waves generated just off the shelf break can propagate only a short distance north before reaching their turning latitude. As an example of what this distance might be, waves with a turning latitude at 40°N (approximately the latitude of N5) and generated at a frequency 3% above the local f would have originated at 38.6° N latitude, approximately 160 km away.

The weather maps covering this time period (Figure 4.6) are useful in determining that this event propagated into the array from offshore,and in explaining why no inertial currents are generated by the PM model. At 0900 on June 5, a low was positioned offshore of the array, with the center almost directly south of N6. The passage of the cold front south of the array would efficiently generate inertial oscillations. By 1200 on June 5 the low had passed to the east of the array, and the increase in energy at N5 and N6 after this time indicates the propagation of the disturbance onto the shelf.

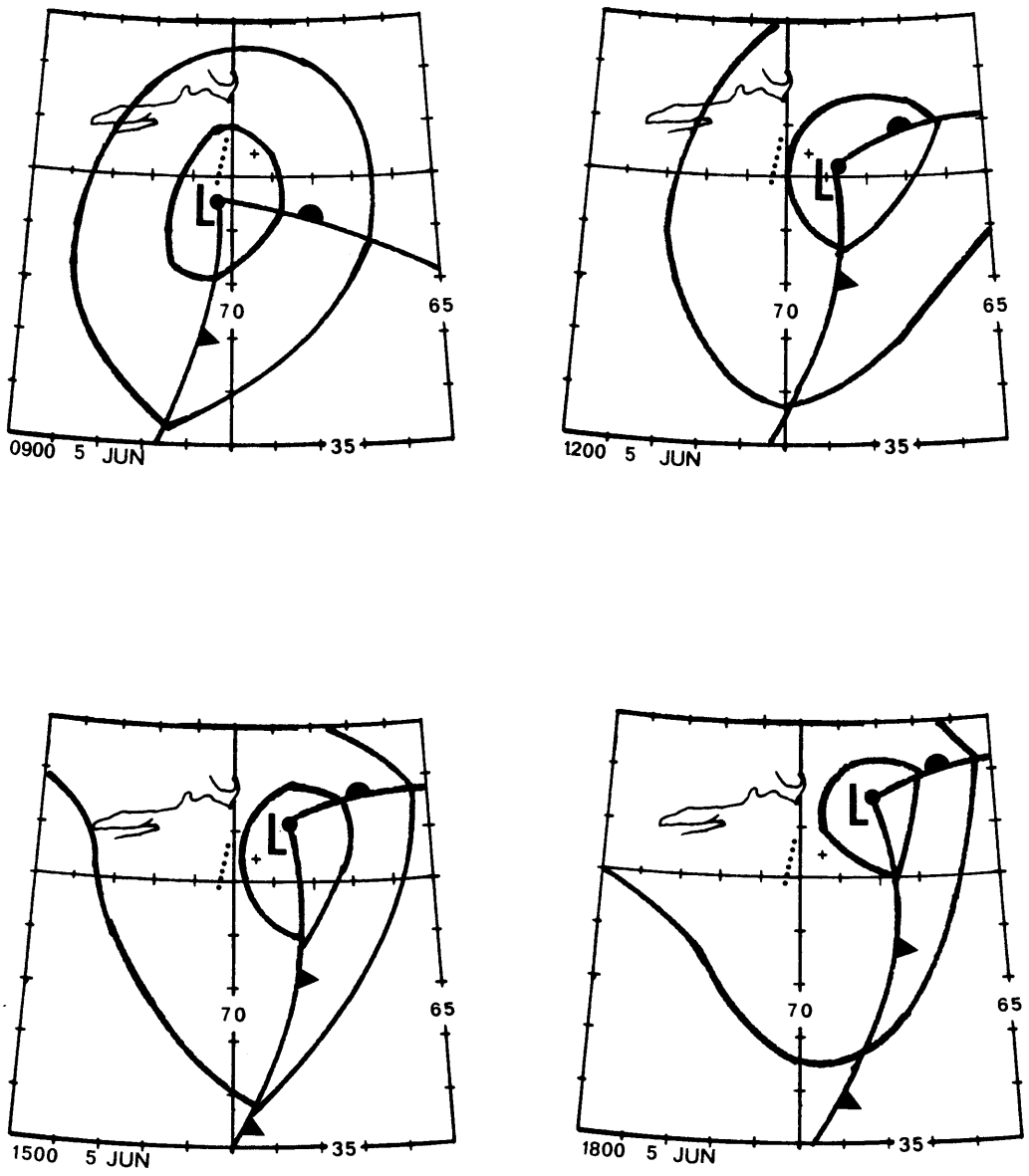

Figure 4.6: Sequence of adaptations of National Weather Service maps showing the passage of a low pressure system associated with event 2 south of the NSFE array.

Note that the center of the low pressure system passed directly over the NLS buoy, so that the winds for this time period do not appear to be favorable for the generation of inertial oscillations. The PM model, which allows only for local generation of inertial currents by the NLS winds, cannot duplicate this event.

The second important deficiency in the PM model is that it does not allow the mixed layer depth to change with time. The equations (4.1) obscure somewhat the role of the mixed layer depth in the excitation and development of inertial oscillations. Following D'Asaro (1985) we can rewrite the PM equations in the following form:

$$\frac{dZ}{dt} + \omega Z = \frac{T}{h}, \tag{4.2}$$

where

$$Z = u + iv,$$

$$T = \frac{\tau^x + i\tau^y}{\rho}, \text{ and}$$

$$\omega = c + if.$$

The steady Ekman transport is given by

$$Z_E = T/\omega h ,$$

and the equation for the inertial oscillations is

$$\frac{dZ_I}{dt} + \omega Z_I = \frac{-dZ_E}{dt} = \frac{-1}{\omega}\frac{d(T/h)}{dt} = \frac{-1}{\omega h}\frac{dT}{dt} - \frac{T}{\omega}\frac{d(1/h)}{dt} \tag{4.3}$$

where

$$Z_I = Z - Z_E.$$

The equations in this form show more clearly that the inertial oscillations are driven by variations in (T/h), although variations in h are only a significant portion of the total mixed layer depth in the case of strong winds. Observations from the west Florida shelf after the passage of a February 1973 cold front show an increase in average mixed layer depth of about 10 m over a time period of half a day. A summertime storm at the same location caused a similar deepening (Price et al., 1978). Data from the Mixed Layer Experiment (MILE) conducted during the fall of 1977 in the northeastern Pacific Ocean show that a rapid increase in the wind coincided with the mixed layer deepening from 8 to 23 m within 4 hours (Davis et al., 1981). During episodes such as these, in which the mixed layer changes by 30 to 200% in a portion of an inertial period, the factor d(1/h)/dt in (4.3) cannot be ignored. At other times, however, the rate of mixed layer deepening is not important, but the amount of deepening over several inertial periods may be important. As the mixed layer deepens the body force is spread over a deeper layer; consequently, weaker mixed layer currents result for the same wind stress.

In order to model the deepening of the mixed layer correctly, information about the atmospheric heating or cooling is needed. The deepening of the mixed layer is then determined by a combination of surface heat flux, shear instability at the base of the mixed layer, and the direct stirring by the wind. After a time equal to approximately one half inertial period, the current vector has rotated away from the wind vector so that the wind is no

longer accelerating the mixed layer currents and deepening due to the shear at the base of the mixed layer stops (deSzoeke and Rhines, 1976; Price et al., 1978). The remaining balance is between the stirring by the wind and the surface heating; this balance is written

$$h \frac{\partial h}{\partial t} = \frac{2\rho}{\Delta\rho} \frac{m_0}{g} u_*^3 - \frac{\alpha Q}{c\Delta\rho} h, \qquad (4.4)$$

(see Davis et al., 1981; and Price et al., 1978), in which $\Delta\rho$ is the density jump across the base of the mixed layer, ρ is a reference density, g is the acceleration due to gravity, m_0 is an efficiency parameter, α and c are the thermal expansibility and heat capacity of water, respectively, at constant pressure, Q is the surface heat flux, and u_* is the friction velocity defined by $u_*^2 = |\tau/\rho|$. Table 4.1 contains monthly averages of surface heat flux, computed from 32 years of data (Goldsmith and Bunker, 1979). Figure 4.7 shows the mixed layer depth as a function of time as calculated from (4.4) using wind stress values of 1 and 5 dynes/cm^2 which are representative of summer and winter conditions, respectively. In each case different values of Q are used to correspond to the months of the winter and summer during which large inertial events occur. These figures are not intended to model the deepening of the mixed layer during any particular event, but rather to show in a general sense that (1) for summer conditions neither the rate of deepening of the mixed layer or the total depth change after several inertial periods is large enough to have an important effect on the current response to a wind event, and (2) mixed layer deepening is more important during the winter months when the wind is stronger and Q

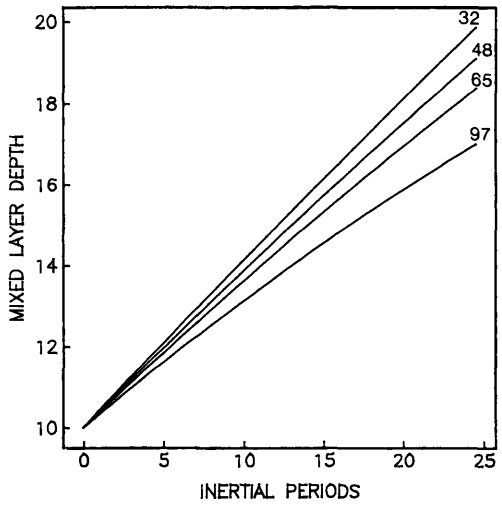

(a)

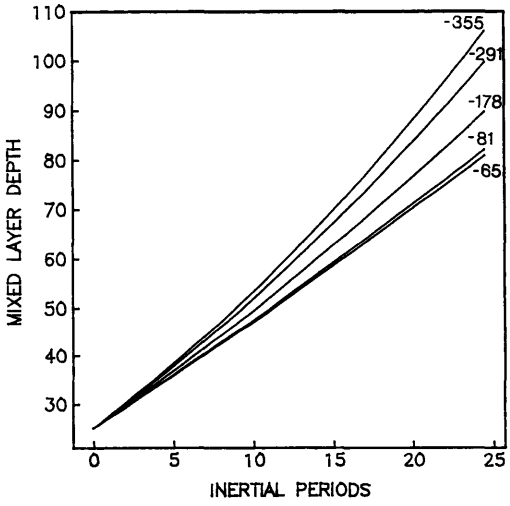

(b)

Figure 4.7: Time series of mixed layer depth as computed from (4.4) representing (a) summer (τ = 1 dyne/cm^2, h_0 = 10 m) and (b) winter (τ = 5 dynes/cm^2, h_0 = 25 m) conditions. Values of surface heat flux associated with each curve are given in units of Watts/m^2. For the purposes of the calculation, the following values were used: $\Delta\rho/\rho = 2 \times 10^{-3}$, $m_0 = .69$, $\alpha = 1.7 \times 10^{-4}$°C^{-1}, $c = 4.1 \times 10^3$ J kg^{-1}. Note the difference in vertical scale between (a) and (b).

is negative. Mixed layer deepening under winter conditions could affect the momentum balance of the PM equations, in which the wind stress is assumed to be spread throughout a mixed layer of constant depth and the removal of energy is proportional to the depth-averaged velocity; certainly it is a factor which should be included in a more sophisticated modelling of the wind generation of inertial oscillations.

In addition to the deficiencies in the model itself, there is a problem with the way the model was used in this case. Pollard (1980) noted that the PM model was sensitive to small variations in the forcing function. Given wind data at three moorings nominally 50 km apart, the PM model produced currents that differed at times by 60° or more in phase and a factor of two in amplitude. It is therefore not surprising that the PM currents are rarely in phase with the observed currents, or that the amplitudes may differ considerably since the wind data is from a buoy approximately 100 km away from the array.

B. The Vertical Structure

The PM model provides no information about the vertical structure associated with an inertial event. The EOF analysis of the previous section suggests that a first baroclinic mode is the dominant form for the response at the inertial frequency in the NSFE data. In order for a mode to form, energy must propagate vertically out of the mixed layer, which will occur due to the divergence of the mixed layer currents. This divergence can be created by variations in the wind stress at the surface or by the presence of a coast which blocks the horizontal flow in the mixed layer and creates

a vertical velocity. By considering these two mechanisms separately, it is possible to contrast the corresponding results.

The solution for wind-forced motions away from the coast can be expanded in normal modes, as was done by Pollard (1970) and Gill (1984). The water column consists of a homogeneous mixed layer over a stratified interior and a flat bottom. To demonstrate the character of the solution, consider the case of an initial distribution of mixed layer currents given by

$$u_i = \sin(\ell y) \tag{4.5}$$
$$v_i = 0$$

which was examined by Gill (1984) for an interior with depth-dependent buoyancy frequency. The variables u and v are orthogonal velocity components in the x and y direction, respectively, the subscript denotes an initial value and ℓ is the wavenumber in the y direction. This initial condition can represent the distribution of mixed layer currents in the wake of a rapidly moving storm. An equivalent problem for an ocean of uniform stratification was done by Pollard (1970). For small times such that the higher frequency modes still appear to be executing pure inertial oscillations, the oscillating part of the currents (neglecting the Ekman transport) is given by

$$\begin{aligned} u &= u_i\ (1-h/H)\cos(ft) \\ v &= -u_i\ (1-h/H)\sin(ft) \end{aligned} \qquad -h < z < 0 \tag{4.6}$$
$$\begin{aligned} u &= u_i\ (-h/H)\cos(ft) \\ v &= -u_i\ (-h/H)\sin(ft) \end{aligned} \qquad -H < z < -h$$

where h is the depth of the mixed layer, H is the total depth of the fluid, and z is positive upward from the ocean surface.

In this limit, the complete solution has the appearance of the first baroclinic mode. However, following Gill (1984), this solution will no longer dominate the vertical structure when the first baroclinic mode becomes 90° out of phase with the pure inertial oscillations. This happens in a time

$$t_n = (\pi/2)\ (\omega_n - f)^{-1},$$

where ω_n is the frequency of mode n. For the purposes of demonstration ω_n can be approximated for an ocean of constant buoyancy frequency as

$$\omega_n^2 = f^2 + \ell^2 c_n^2 = f^2 + \ell^2\ (N^2H^2/n^2\pi^2).$$

For $N^2 = 2 \times 10^{-4} s^{-2}$, H = 100 m, and $\ell^2 = (2\pi/150\ km)^{-2}$, the frequency of the first mode is about 2% above f and the time for the first mode to separate out is 12 inertial periods. This is longer than the duration of any single event, and it is therefore not surprising that the first mode dominates in the observations; in fact it would be more difficult to explain the appearance of a higher mode structure. Note that the dominance of the first baroclinic mode is independent of the stratification below the mixed layer. The calculation also implies that the dominance of the first baroclinic mode requires horizontal wavelengths ~100 km or greater; smaller wavelengths result in a higher frequency for the first baroclinic mode.

In the deep ocean, the inertial currents below the mixed layer are essentially zero, but over the shelf the facter h/H is bigger -- as much as 0.25 for a 25 m mixed layer in 100 m of water, for example, and it will increase as the depth decreases toward the coast. Notice in (4.6) that for a given total depth the surface-intensification increases as the mixed layer depth decreases. In a general sense, this result is consistent with the

NSFE data -- during the summer the mixed layer depth is, on average, less than the mixed layer depth during the winter; consequently, the response in the summer is more surface-intensified. More specifically, however, we can ask if the upper and lower layer currents are in the ratio $(H - h)/h$. The upper and lower layer velocities were estimated from the amplitudes of the complex demodulation analysis for each event at N4 and N5, and the mixed layer depth was then estimated by assuming that the above ratio was approximately correct. Table 4.2 compares the mixed layer depths estimated using the ratio of upper to lower layer velocities with mixed layer depths estimated from the hydrographic data. Estimates of mixed layer depth computed by using the ratio method are consistently greater than those estimated from the hydrographic data. No definitive explanation is offered for this. Note, however, that mixed layer depths estimated from the hydrographic data are subject to much error, and that the concept of a slab-like mixed layer is based on an assumption about the vertical distribution of eddy viscosity, i.e., that the eddy viscosity is very high over the depth of the density mixed layer and is zero below this depth. In reality, this distribution may be smoother and the base of the constant density layer may not define the depth at which the stress, and therefore the upper layer currents, vanish. It is also possible that a reduction in the expected surface-intensification is due to propagation over the sloping topography, although a distortion of the flat-bottom modes should be accompanied by a vertical component of group velocity which is not evident in the data. The data may not be adequate to resolve a slight vertical propagation of energy, so the possibility is not to be dismissed. Further discussion of the effects of bottom topography is given in part (D).

A coastline which interrupts the flow in the mixed layer causes vertical energy propagation even in the present of a wind with no horizontal variation. The solution to wind-forced motions over a flat-bottom ocean in the presence of a coast was treated in a numerical model by Kundu et al. (1983) using an expansion in normal modes. If only two modes are considered then the solution reduces to that for a two-layer ocean which was studied by Millot and Crepon (1981) and Pettigrew (1981). Recall that in a two-layer ocean without a coastline a wind stress with no horizontal variation will spin up the surface layer while the bottom layer remains motionless (the PM model); however, the presence of a coastline changes the nature of the response substantially through the constraint of no flow normal to the boundary. The coast appears as a source for near-inerital waves which are generated in order to satisfy the boundary condition. In a two-layer fluid the barotropic and baroclinic modes propagate seaward with speeds

$$c_0 = \sqrt{[g(h_1 + h_2)]} \text{ and}$$

$$c_1 = \sqrt{[g'h_1h_2/(h_1 + h_2)]}$$

respectively, h_1 being the upper layer depth, h_2 the lower layer depth, g gravitational acceleration, and g' reduced gravity. Over a shelf 100 m deep with a 10 m thick upper layer and a value of $g' = 10^{-3}g$, these speeds are $c_0 = 110$ km/hr and $c_1 = 1.1$ km/hr. Clearly the barotropic mode travels so fast that over the width of the shelf its arrival will not be discernable from the directly wind-forced current in the upper layer. The baroclinic response, however, could take many hours to several days to cover the part of the shelf occupied by the NSFE array. In fact, a baroclinic mode which is reflected from the coast would not be expected to reach mid- to outer-shelf locations. To see this, suppose a baroclinic front traveling at speed

c_1 = 1 km/hr must travel 100 km to reach N5 or N6 at the NSFE array. The decay time scale of ~1 day which was calculated above suggests that the front will propagate only about a quarter of this distance before being dissipated by bottom friction, a result which will vary somewhat depending on the layer depths and the magnitude of the velocity in the lower layer. Note that assuming a depth of 100 m minimizes the effects of bottom friction in shallower regions close to the coast. Conditions of strong stratification would increase the speed of the wave; however, under rather extreme conditions in which the mixed layer depth reaches 25 m and $g'/g = .004$, the phase speed of the baroclinic wave is 3.1 km/hr, and the wave would still be highly dissipated by the time it reached the outer shelf.

Given the slow propagation of the internal modes, the response at mid to outer shelf locations due to the reflection of waves at the coast will be dominated by the sum of the directly wind-driven mixed layer currents (the pure inertial oscillations) and the barotropic mode. The barotropic mode contains contributions from all frequencies and all horizontal wavenumbers. The high frequency short waves have the highest group velocities and therefore collect behind a "front" which propagates away from the coast with speed c_0. For times satisfying $t >> x/c_0$ the long waves are left behind and the frequency of the mode approaches f. The upper and lower layer velocities in this limit are easily derived from the total solution as given by Pettigrew (1981). If the system is forced with a wind stress $\tau_0^x \delta(t)$, where δ is the Dirac delta function, then the velocities are:

$$u_1 = \frac{\tau_0^x}{\rho h f} \frac{H - h}{H} \sin(ft) ,$$

$$v_1 = \frac{-\tau_0^x}{\rho h f} \frac{H - h}{H} [1 - \cos(ft)] ,$$

$$u_2 = \frac{-h}{H - h} u_1 ,$$

$$v_2 = \frac{-h}{H - h} v_1 ,$$

where the subscripts 1 and 2 denote the upper and lower layer velocities, respectively. As in the previous example in which the wind stress varied horizontally, the velocity field has the appearance of a first baroclinic mode, and the ratio of the upper to the lower layer velocities is (H - h)/h. Also in analogy with the previous example, this result, which was derived by considering a two-layer ocean, is valid for more general stratification and all times of interest, at least at the southernmost moorings N3-N6. Continuous stratification requires the presence of higher modes near the coast in order to satisfy the boundary condition, but these have negligible effect on the response at the outer shelf if the argument presented concerning the effects of friction is valid.

The higher modes near the coast do contribute to the "coastal inhibition" effect (Kundu et al., 1983), which may explain the drop in energy along the array as the coast is approached. Because a condition of no normal flow must be satisfied, incident and reflected waves at the coast must cancel each other exactly at this point and nearly exactly at short distances from this point. Note that this is also true in the two-layer case

in which there is only one baroclinic mode. Because of the sloping topography, the mixed layer probably intersects the bottom at some distance seaward of the true coastline. It is not clear exactly what boundary condition is satisfied at this point, but at least partial reflection should take place and it may well occur near enough to the NSFE array to cause the decrease in energy at the northern moorings. Because the mixed layer is deeper during the winter, it should intercept the bottom at a more seaward location than during the summer, which might explain why the data show that the the two-layer structure extends to N2 during the summer but only as far as N3 during the winter.

The presence of a two-layer type of structure in the NSFE data can be adequately explained by either of the two mechanisms described above, i.e. reflection from the coast of uniformly surface-forced mixed layer currents, or surface forcing by a horizontally varying wind. In theory, the two mechanisms could be distinguished at outer shelf locations by the vertical structure of the temperature oscillations, which would be barotropic for a barotropic mode reflected from the coast and baroclinic for a baroclinic mode forced by Ekman pumping. However, the vertical velocities are so small, even for a baroclinic mode, that in practice no useful information is gained by looking at the temperature spectra. The maximum vertical displacement at the interface for the first baroclinic mode is given by (Gill, 1984)

$$h_{max} = 2\ell h f^{-1} \left| u_i \right| ,$$

which is equal to about 1 m at the NSFE latitudes if $h = 10$ m, $\ell = 2\pi/150$ km, and the magnitude of the initial mixed layer currents is 10 cm/s. It is therefore not surprising that, although a few instruments show small

inertial peaks in the temperature data (not statistically significant), no vertical structure in temperature emerges from the available information. In reality, the vertical structure is probably a combination of the two effects, perhaps with reflection dominating at the inner shelf and Ekman pumping at the outer shelf.

C. Effect of the Mean Currents

Figure 4.5 shows that low-frequency alongshelf currents are quite strong during NSFE, often reaching values of 30 cm/s. In addition, the passage of Gulf Stream rings (GSRs) through the southern extent of the array during the summer created periods of strong geostrophic shear (rings 79-A, 79-B and 78-I have been identified, in the nomenclature of Fitzgerald and Chamberlin, 1981). In Figure 4.5 the signature of these rings is a strong eastward flow at N6(10) which rotates from northeast to southeast as the ring goes by. The effect of these highly sheared mean currents on the inertial oscillations is expected to be twofold: (1) the variable mean shear shifts the effective inertial frequency unevenly along the shelf, causing phase differences to accumulate in the mixed layer oscillations thereby reducing their horizontal length scales, and (2) the strong mean flows can doppler-shift the frequency observed at the current meters. Both of these factors have implications for the horizontal wavelength and direction of propagation of the inertial oscillations.

As pointed out in section III, there is some ambiguity in determining the horizontal wavelengths and direction of phase propagation (onshore or offshore) of the inertial events. Weather maps show that fronts pass southeastward across the array at speeds from ~20 to ~50 km/hr. Estimates of

horizontal wavelength based on a phase speed equal to the translation speed of the front would be 370 to 930 km, given the above range. This would indicate that the horizontal wavelengths are quite large, and that phase propagation is offshore with the front. However, phase information from the complex demodulation suggested that offshore propagation during event 1, for example, would require a small horizontal wavelength (Table 3.4 and Figure 3.6). A possible resolution of this contradiction is that large scale inertial oscillations initially generated by the wind can be converted to smaller scale motions by interaction with a mean flow with variable shear (Rubinstein and Roberts, 1986). This mechanism is more likely to be important during the summer period since the passage of GSRs through the southern extent of the array created highly sheared mean currents. The time series in Figure 4.5 were used to calculate estimates of the shear between the 10 m instruments during the summer period. The shear exhibits variability on the scale of the spacing of the moorings, 20-30 km. The results of Rubinstein and Roberts (1986) show that variability in the shear of the mean flow on this scale starts inertial pumping with spatial scales O(10 km), causing initially large scale inertial oscillations to break up into motions with much smaller length scales. In their analysis the relative vorticity varied between ±5% of the local inertial frequency; this corresponds to approximately $\pm 5 \times 10^{-6} s^{-1}$ at the location of the NSFE array. Figure 4.8 confirms that the shear can often vary by this amount over the distance between two moorings. Therefore, the variable mean shear could be important in converting large-scale inertial oscillations associated with atmospheric fronts to smaller scales propagating primarily offshore; this is consistent with one interpretation of the phase information during events 1 and 5 (Table 3.7).

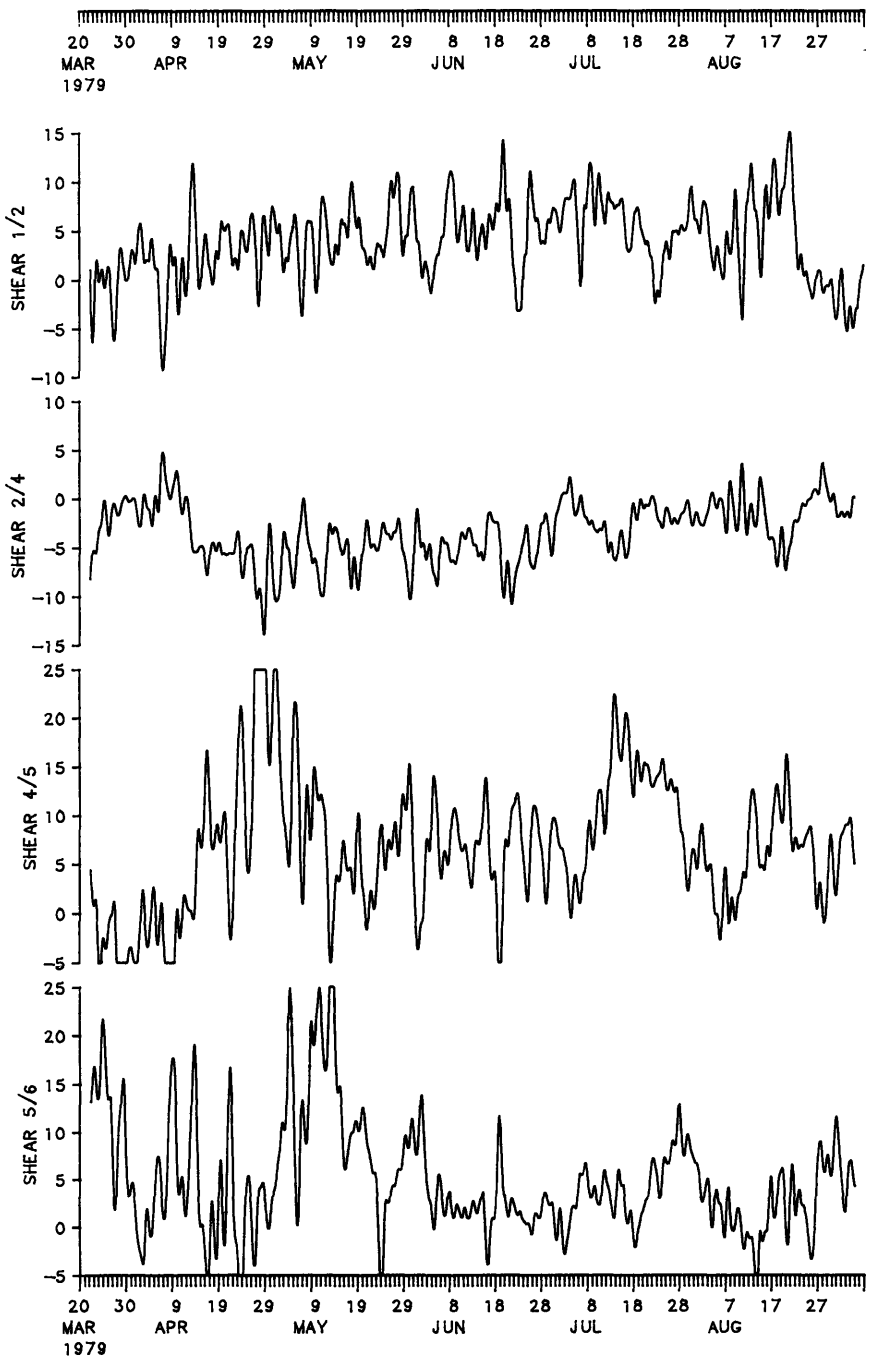

Figure 4.8: Time series of shear between 10 m instruments during the summer period. Units are $s^{-1} \times 10^{6}$. Shear was computed from finite differences of currents filtered with a low-pass filter with a half-amplitude period of 33 hours.

Figure 4.5 shows that the mean alongshelf currents are much greater than the mean cross-shelf currents. Without any information about variability along the coast it is impossible to make definitive statements about propagation in this direction. For Doppler shifting to be important, however, there must be some propagation perpendicular to the array, along the axis of the large mean flows. The magnitude of the Doppler shift depends on the projection of the wavenumber onto the mean flow, $k_x = 2\pi \sin\phi/\lambda_H$, where ϕ is the angle the wavenumber makes with the axis of the array. This means that a significant Doppler shift can occur if (1) a large scale wave is propagating at a large angle to the array, or (2) a small-scale wave is propagating at a small angle to the array. A simple calculation gives an idea of the wavelengths and angles of propagation required. Consider as a simplification a plane wave with an intrinsic frequency close to f. Mean alongshelf currents on the outer shelf often reach values of 30 cm/s, but to be conservative a mean alongshelf current of $U = 10$ cm/s will be used. The frequency observed at a current meter is $\omega = \underline{k} \cdot \underline{U} + f$. If the wave has a wavelength of 20 km, then to produce a Doppler shift $k_xU = 3 \times 10^{-6}s^{-1}$ (~3% of f) requires $\phi = 5.5°$. Thus, the observed subinertial frequencies could easily be produced by a Doppler shift even if the wave is propagating primarily perpendicular to the coast, if the wavelength is small. The phase speed can be directed onshore or offshore, but the wave must be propagating slightly westward, since the strong mean flows at the outer shelf are primarily eastward (Figure 4.5). Now presume that the waves are propagating with an atmospheric front southeastward at an angle 45° measured counterclockwise from the axis of the array. In order to produce the

same Doppler shift in this case, a wavelength of 150 km is required. Larger wavelengths which are in the range of those calculated from the translation speeds of the fronts would produce smaller Doppler shifts from about 1% to .5% of f. Note, however, that waves propagating with the atmospheric front would be propagating with, rather than against, the strong currents of the GSRs and the doppler-shifted frequency would be superinertial.

The observed frequency shifts during the events cannot be used to determine with certainty the horizontal wavelength and direction of propagation. Mean currents during the winter period are highly variable, so that the direction of propagation required to produce the observed Doppler shift during either of events 6 or 7 is difficult to determine. Events 1, 3 and 5 coincide with the passage of a GSR near the array. Events 3 and 5 show superinertial frequency shifts (Tables 3.2 and 3.3), which could be due to a Doppler shift or to an increase in the effective Coriolis parameter since the relative vorticity of the sheared mean flow at N4, N5, and N6 is positive. Event 1 shows a subinertial frequency shift which can only be explained if the disturbance is propagating westward. It has been argued that this event probably has a small horizontal wavelength and propagates offshore; in this case the angle of propagation relative to the array can be quite small and still produce the observed Doppler shift. Event 4, which also shows a subinertial shift, occurs just prior to the passage of a GSR at a time when the mean currents are quite weak, so the Doppler effect cannot be offered as an explanation. Thus, while it seems clear that the mean currents can have an effect on the Eulerian frequency and the horizontal wavelength of the inertial oscillations, the NSFE data are not sufficient to assess the extent of this effect.

D. The Effects of Bottom Topography

The effect of the sloping bottom topography on the vertical structure at the NSFE array is not great, as evidenced by the fact that the observations still strongly resemble a first baroclinic flat-bottom mode. Previous work indicates what the expected changes would be if the bottom topography were an important influence. In a "wedge" of constant buoyancy frequency, the modes propagating up and down the slope exhibit a bottom intensification as the coast is approached (Wunsch, 1968, 1969). This is accompanied by a propagation of energy downward and seaward if the waves are propagating down the slope, and upward and toward the coast if the waves are propagating up the slope. The NSFE data do not show bottom intensification, although a reduction in the expected surface-intensification might be attributed to the effect of the sloping bottom. There is also no clear evidence of vertical energy propagation, which manifests itself as a continuous change in phase with depth, although given the O(20 m) vertical spacing of the instruments a slight vertical energy propagation would be missed. Because the inertial oscillations are forced at the surface and are therefore surface-intensified with small near-bottom velocities, the effect of bottom topography on the structure of the mode is minimized. There is observational evidence that a stronger bottom slope can modify the flat-bottom modes in the expected manner. Observations off the coast of Oregon where the slope is $\sim 7 \times 10^{-3}$ (as compared to $\sim 2 \times 10^{-3}$ between N1 and N4) do not show a clear modal structure and are not as strongly surface-intensified as those of NSFE, and there does seem to be a downward vertical component of group velocity (Kundu, 1976). Although stratification is also a factor, the sloping bottom appears to

exert a stronger influence off the coast of Oregon than in the Middle Atlantic Bight.

One other aspect of the sloping bottom topography which should be mentioned for completeness is that it allows the shelf to act as a waveguide, propagating energy along the coast in the form of coastally-trapped waves. In general, coastally-trapped waves exist at subinertial frequencies, although for a critical value of the stratification parameter $S = NH/fL$, where H is the deep ocean depth, L is the width of the shelf and slope region, and N is the buoyancy frequency, the dispersion curves cross f and there exists a near-inertial frequency limit (Chapman, 1983). The vertical structure can be computed in this near-inertial limit (Brink and Chapman, 1985) for arbitrary bottom topography and vertical stratification. For the NSFE bottom topography and an idealization of the buoyancy profile suggested by the hydrographic sections at various times during the experiment, it was found that the dispersion curves can cross f. However, the first zero crossing in velocity is found well down on the slope and for no reasonable vertical dependence of the buoyancy frequency could it occur between 10 and 50 m depth as is shown in the observations. Therefore, coastally-trapped waves are not expected to be a major contribution to the near-inertial energy in the NSFE currents.

E. Summary

Using a very simple one dimensional mixed layer model it was shown that much of the inertial energy observed during NSFE can be traced to winds at the surface. While the model itself is too simple to give anything

but the most rudimentary results, consideration of some of its deficiencies indicates that the NSFE data are inadequate to test a more sophisticated model. The spatial structure of the wind as well as its time dependence is very important in the generation of the inertial oscillations. Information on mixed layer deepening is also needed, or, if this is to be considered as part of the response, surface heat flux is necessary to compute the deepening accurately. This information was not available for the present work.

This section has shown what some of the effects of the boundaries (the coast, the sloping bottom, and the open boundary at the shelf break) on the inertial wave field over the shelf might be. Discussion of event 2 in some detail confirmed that the open boundary at the shelf break can, at times, act as a source for the near-inertial energy over the shelf. Reflection at the coastal wall accounts for the drop in energy at the northern extent of the array. The bottom boundary interrupts the downward propagation of energy from the mixed layer, setting up a standing wave type of response. The fact that the bottom boundary is sloping seems to be of minimal importance in the NSFE data, since the observed vertical structure strongly resembles that predicted for a flat bottom.

Finally, mean flow characteristics which might affect the horizontal wavelength (the geostrophic shear) or define the direction of propagation (the Doppler shift) were discussed. There is still too little information to determine unambiguously the horizontal wavelength or phase speed in most cases, although a small disturbance propagating phase offshore seems to be the only interpretation consistent with all the available information during event 1.

V. Summary

Current meter data obtained during the Nantucket Shoals Flux Experiment show a prominent peak in the clockwise-rotating component of the energy in the inertial frequency band, indicating the presence of energetic inertial oscillations. A least squares fit to a sinusoid at the inertial frequency over successive segments of the data yields a time series of the amplitude at the inertial frequency over the course of the year-long experiment. This time series shows quite clearly that the near-inertial energy is concentrated in intermittent events with time scales on the order of 10 days and that these events are highly coherent through the mixed layer over the mid and outer shelf.

It was proposed that the NSFE data set could be used to determine a range of wavelengths that would be particular to the forcing functions found in the Middle Atlantic Bight. Although coherences in the horizontal are generally high, there are no significant phase differences. It may be more appropriate to estimate wavelength and phase speed on an event-by-event basis, as they are likely to change due to different forcing functions, stratification, and mean flow characteristics. However, even when relatively stable phase lags are found between instruments over the course of a single event, there remains an ambiguity since the horizontal spacing of the moorings is not small enough to resolve the short wavelengths. Because the vertical structure is dominated by the first baroclinic mode, the dispersion relation can be used to establish that freely-propagating near-inertial waves should have horizontal wavelengths on the order of 100 km. A similar estimate results from consideration of waves forced at the surface by a

horizontally divergent wind stress. Some questions of horizontal wavelength and phase speed remain unanswered, however. Phase information suggests that at least one event is characterized by a small, O(20 km), wavelength. In addition, the direction of propagation appears to be, at times, contrary to that expected if the waves were forced by atmospheric fronts passing over the array.

The vertical structure appears to be not only well-established by this data set, but also quite consistent through all the events in inertial energy. This was presented most concisely by a frequency-domain empirical orthogonal function analysis, which showed a two-layer structure with surface-intensified velocities, and upper and lower layer velocities 180° out of phase. The two-layer structure is consistent across the outer shelf, although it decays in amplitude toward the coast, probably due to waves that are reflected there in order to satisfy the boundary condition. That this two-layer structure is representative of the response at the inertial frequency in general, not just during a few of the events, was confirmed by a time-domain EOF analysis. The time series of the amplitude of the two-layer structure showed each of the events in inertial energy that appeared when the time dependence of the inertial energy in the current data was examined using a complex demodulation technique. It appears that the question of the vertical structure of the inertial oscillations could be addressed adequately with the NSFE data.

Finally, it was hoped that the NSFE array, positioned perpendicular to the coast and across the shelf break, could provide some insight into the effect of the deep ocean near-inertial wave field on the inertial energy

over the shelf through the open boundary at the shelf break. In general, this effect seems to be small and most of the inertial energy over the shelf can be accounted for in terms of local forcing at the surface. One event in particular, however, seemed to show quite clearly that under certain conditions inertial oscillations forced seaward of the shelf break could propagate onto the outer shelf. These oscillations were also wind-forced, and their source was not far (O(200) km) from the shelf break, which is as expected. While there are other vertical scales and sources other than the wind in the deep ocean, the larger vertical scales will be reflected at the continental slope, so propagation through the shelf break boundary will be possible only for the surface-intensified, wind-driven disturbances, and because of the slowness of propagation of high vertical wavenumber near-inertial waves, the region of the deep ocean which can influence the shelf is restricted to a few hundred kilometers.

Acknowledgements

This work was supported by the National Science Foundation grant OCE84-17769. I would like to thank my committee members: Ken Brink, Paola Rizzoli, Joe Pedlosky, and Robert Beardsley, as well as my thesis advisor, David Chapman. Discussions with Mike McCartney, Eric Kunze and Carl Wunsch were extremely helpful.

References

Anderson, I., A. Huyer, and R. L. Smith, 1983: Near-inertial motions off the Oregon coast. Journal of Geophysical Research, 88(C10), 5960-5972.

Beardsley, R. C., D. C. Chapman, K. H. Brink, S. R. Ramp, and R. Schlitz, 1985: The Nantucket Shoals Flux Experiment (NSFE79), Part 1: A basic description of the current and temperature variability. Journal of Physical Oceanography, 15, 713-748.

Brink, K. H., and D. C. Chapman, 1985: Programs for computing properties of coastal-trapped waves and wind-driven motions over the continental shelf and slope. Woods Hole Oceanographic Institution Technical Report WHOI-85-17, 99 pp.

Chapman, D. C., 1983. On the influence of stratification and continental shelf and slope topography on the dispersion of subinertial coastally trapped waves. Journal of Physical Oceanography, 13, 1641-1652.

Chelton, D. B., 1983. Effects of sampling errors in statistical estimation. Deep-Sea Research, 30(10A), 1083-1103.

D'Asaro, E. A., 1985: The energy flux from the wind to near-inertial motions in the surface mixed layer. Journal of Physical Oceanography, 15, 1043-1059.

Davis, R. E., R. de Szoeke, D. Halpern, and P. Niiler, 1981: Variability in the upper ocean during MILE. Part 1: The heat and momentum balances. Deep-Sea Research, 28A, 1427-1451.

Denbo, D. H., and J. S. Allen, 1984: Rotary empirical orthogonal function analysis of currents near the Oregon coast. Journal of Physical Oceanography, 14(1), 35-46.

de Szoeke, R. A., and P. B. Rhines, 1976: Asymptotic regimes in mixed-layer deepening. Journal of Marine Research, 34, 111-116.

Eriksen, C., 1982. Observations of internal wave reflection off sloping bottoms. Journal of Geophysical Research, 87, 525-538.

Fitzgerald, J. L., and J. L. Chamberlain, 1981: Anticyclonic warm core Gulf Stream eddies off the northeastern United States in 1979. Anna. Biologig., Copenhagen, 36, 44-51.

Fu, L., 1981. Observations and models of inertial waves in the deep ocean. Reviews of Geophysics and Space Physics, 19, 141-170.

Garrett, C., and W. Munk, 1979: Internal waves in the ocean. Annual Reviews of Fluid Mechanics, 11, 339-369.

Gill, A., 1982: Atmosphere-Ocean Dynamics. Academic Press, Inc., London.

Gill, A. E., 1984: On the behavior of internal waves in the wakes of storms. Journal of Physical Oceanography, 14, 1129-1151.

Goldsmith, R. A., and A. F. Bunker, 1979: WHOI Collection of Climatology and Air/Sea Interaction (CASI) Data. Woods Hole Oceanographic Institution Technical Report WHOI-79-70.

Gonella, J., 1972: A rotary-component method for analysing meteorological and oceanographic vector time series. Deep-Sea Research, 19, 833-846.

Hayes, S. P., and D. Halpern, 1976: Observations of internal waves and coastal upwelling off the Oregon coast. Journal of Marine Research, 34, 247-267.

Johnson, C. L., J. C. Van Leer, and C. N. K. Mooers, 1976: A cyclosonde view of coastal upwelling. Journal of Physical Oceanography, 6, 556-574.

Johnson, W. R., 1981: The propagation of tidal and inertial waves in the upwelling region off Peru. In: Coastal Upwelling, Francis A. Richards, editor, Coastal and Estuarine Sciences, 1, American Geophysical Union, Washington, D.C., pp. 79-86.

Kundu, P. K., 1976: An analysis of inertial oscillations observed near the Oregon coast. Journal of Physical Oceanography, 6, 879-893.

Kundu, P. K., and J. S. Allen, 1976: Some three-dimensional characteristics of low-frequency current fluctuations near the Oregon coast. Journal of Physical Oceanography, 6, 181-199.

Kundu, P. K., S. Y. Chao, and J. P. McCreary, 1983: Transient coastal currents and inertio-gravity waves. Deep-Sea Research, 30(10A), 1059-1082.

Kunze, E., and T. Sanford, 1986. Near-inertial wave interactions with mean flow and bottom topography near Caryn Seamount. Journal of Physical Oceanography, 16, 109-120.

Lai, D. Y., and T. B. Sanford, 1986: Observations of hurricane-generated, near-inertial slope modes. Journal of Physical Oceanography, 16, 657-666.

Large, W. S., and S. Pond, 1981: Open ocean momentum flux measurements in moderate to strong winds. Journal of Physical Oceanography, 11, 324-336.

Leaman, K., 1976. Observations on the vertical polarization and energy flux of near-inertial waves. Journal of Physical Oceanography, 6, 894-908.

Leaman, K., and T. Sanford, 1975. Vertical energy propagation of inertial waves: A vector spectral analysis of velocity profiles. Journal of Geophysical Research, 80, 1975-1978.

LeBlond, P. H., and L. A. Mysak, 1978: Waves in the Ocean. Elsevier Scientific Publishing Company, Amsterdam, The Netherlands.

Mayer, D. A., H. O. Mofjeld, and K. D. Leaman, 1981: Near-inertial internal waves observed on the outer shelf of the Middle Atlantic Bight in the wake of Hurricane Belle. Journal of Physical Oceanography, 11, 87-106.

Millot, C., and M. Crepon, 1981: Inertial oscillations on the continental shelf of the Gulf of Lions -- observations and theory. Journal of Physical Oceanography, 11, 639-657.

Munk, W., and N. Phillips, 1968: Coherence and band structure of inertial motion in the sea. Reviews of Geophysics, 6, 447-472.

Perkins, H. T., 1970: Inertial oscillations in the Mediterranean. Ph.D. Thesis, M.I.T./W.H.O.I. Joint Program, 153 p.

Perkins, H., 1972: Inertial oscillations in the Mediterranean. Deep-Sea Research, 19, 289-296.

Pettigrew, N. R., 1981: The dynamics and kinematics of the coastal boundary layer off Long Island. Ph.D. Thesis, M.I.T./W.H.O.I. Joint Program, 261 p.

Pollard, R. T., 1970: On the generation by winds of inertial waves in the ocean. Deep-Sea Research, 17, 795-812.

Pollard, R. T., 1980: Properties of near-surface inertial oscillations. Journal of Physical Oceanography, 10, 385-398.

Pollard, R. T., and R. C. Millard, Jr., 1970: Comparison between observed and simulated wind-generated inertial oscillations. Deep-Sea Research, 17, 813-821.

Price, J. F., C. N. K. Mooers, and J. C. Van Leer, 1978: Observation and simulation of storm-induced mixed-layer deepening. Journal of Physical Oceanography, 8, 582-599.

Prinsenberg, S. J., W. L. Wilmot, and M. Rattray, Jr., 1974: Generation and dissipation of coastal internal tides. Deep-Sea Research, 21, 263-281.

Rubinstein, D. M., and G. O. Roberts, 1986: Scattering of inertial waves by an ocean front. Journal of Physical Oceanography, 16, 121-131.

Sanford, T., 1975. Observations of the vertical structure of internal waves. Journal of Geophysical Research, 80, 3861-3871.

Schott, F., 1971. Spatial structure of inertial-period motions in a two-layered sea, based on observations. Journal of Marine Research, 29, 85-102.

Thomson, R. E., and W. S. Huggett, 1981: Wind-driven inertial oscillations of large spatial coherence. Atmospheric-Ocean, 19, 281-306.

Webster, F., 1968: Observations of inertial-period motions in the deep sea. Reviews of Geophysics, 6, 473-490.

Webster, F., and N. P. Fofonoff, 1967: A compilation of moored current meter observations, Vol. 3. Woods Hole Oceanographic Institution Technical Report 67-66, 105 pp.

Wright, W. R., 1983: Nantucket Shoals Flux Experiment data report I: Hydrography. NMFS, Northeast Fisheries Center, Woods Hole, MA; NOAA Tech. Memo. NMFS-F/NEC-23, 108 pp.

Wunsch, C., 1968: On the propagation of internal waves up a slope. Deep-Sea Research, 15, 251-258.

Wunsch, C., 1969: Progressive internal waves on slopes. Journal of Fluid Mechanics, 35, 131-144.

Table 3.1: Variance of the clockwise rotating component in the inertial freqency band. Units are $[cm/s]^2$. Where two estimates are listed, the time series are broken into two pieces as indicated in Figure 2.2.

Instrument	Summer KE	Winter KE
N1(10)	3.7*	
N1(32)	1.8*	1.1*
N2(10)	25	
N2(32)	4.3	9.4, 1.5*
N2(52)	2.1	19, 1.2*
N2(65)	.82*	2.3, .52*
N3(10)		**
N3(32)	8.6	4.1
N3(72)	7.9	10
N4(10)	43	
N4(29)		13
N4(59)	9.4	
N4(89)	8.1	13
N5(10)	46	
N5(28)	17	25
N5(88)	6.2	
N5(118)	5.9	9.2
N5(183)	5.5	
N6(10)	61	42

* Energy is inertial band is not significantly above background levels at 95% confidence.

** The length of the time series was not sufficient to resolve the inertial and tidal peaks.

COMPLEX DEMODULATES: SUMMER PERIOD

Table 3.2: Summary of 4 high amplitude inertial events during the summer period at 10 m instruments. ε is the deviation from the demodulation frequency 0.054 cph; e.g. signal frequency $\omega = 0.054 + \varepsilon$ cph.

	EVENT 1	EVENT 2	EVENT 3	EVENT 4
Inst N6(10)				
maximum amplitude (cm/s)	15	22	11	28
duration	April 30- May 9	June 2- June 11	July 2- July 12	Aug 9- Aug 16
estimate of ε (cph)	-.0015	0.0	.0003	-.001
Inst N5(10)				
maximum amplitude (cm/s)	13	15	15	30
duration	April 29- May 9	June 2- June 11	July 4- July 11	Aug 6- Aug 15
estimate of ε (cph)	-.001	-.0003	.0003	-.0006
Inst N4(10)				
maximum amplitude (cm/s)	15	12	12	25
duration	May 3- May 9	May 28- June 8	July 7- July 10	Aug 9- Aug 17
estimate of ε (cph)	-.0006	-.0004	-.0009	-.0009
Inst N2(10)				
maximum amplitude (cm/s)	8			16
duration	April 29- May 8			Aug 9- Aug 15
estimate of ε (cph)	-.0015			-.001

COMPLEX DEMODULATES: WINTER

Table 3.3: Summary of 3 high amplitude inertial events during the winter period at shallowest instruments available, moorings 4, 5 and 6. ε is the same as in Table 3.2.

	EVENT 5	EVENT 6	EVENT 7
Inst N6(10)			
maximum amplitude (cm/s)	24	18	18
duration	Sept 20-Sept 30	Oct 7-Oct 12	Dec 7-Dec 12
estimate of ε (cph)	.0003	-.001	.0005
Inst N5(28)			
maximum amplitude (cm/s)	22	17	10
duration	Sept 20-Sept 30	Oct 7-Oct 13	Dec 7-Dec 13
estimate of ε (cph)	.0003	-.001	.001
Inst N4(29)			
maximum amplitude (cm/s)	12	10	8
duration	Sept 21-Sept 30	Oct 7-Oct 10	Dec 7-Dec 12
estimate of ε (cph)	.0004	-.0004	.001
Inst N3(10)			
maximum amplitude	26	10	
duration	Sept 16-Sept 30	Oct 7-Oct 12	
estimate of ε (cph)	.0001	-.001	

Table 3.4: Coherence and phase estimates in inertial frequency band for the summer period. Frequency band is centered on 0.054 cph with a bandwidth of 0.0025 cph. Only values significant at 95% confidence are shown. A positive phase indicates that the column instrument leads the row instrument.

	N2(10)	N2(65)	N3(32)	N3(72)	N4(10)	N4(59)	N5(10)	N5(88)	N5(118)	N6(10)
N1(10)	.56 29±47									
N2(10)				.61 -138± 40	.58 26± 44					
N2(32)			.53 -18± 51							
N2(52)		.63 43± 38		.62 14± 39			.58 -157± 44			
N3(72)					.55 167± 48	.56 8±47	.55 -174± 49	.55 13± 49		
N4(10)						.69 -162± 31	.74 14±27			.55 5±49
N4(59)							.57 180±45	.71 -3±29		
N4(89)								.68 1±32	.75 11±26	
N5(10)								.58 179±44		.69 -1±31
N5(88)									.75 16±26	

Table 3.5: Coherence and phase estimates in the inertial frequency band for the winter period. Frequency band is centered on 0.054 cph with a bandwidth of 0.0025 cph. Only values significant at 95% confidence are shown. A positive phase indicates that the column instrument leads the row instrument.

	N3(72)	N4(29)	N4(89)	N5(28)	N5(118)	N6(10)
N3(32)	.74 -171± 27	.78 6.4±24		.80 14.5± 21	.59 -165± 42	.70 18.8± 31
N3(72)		.79 177± 23	.73 -1±27	.85 -173± 18	.76 2.8± 25	.83 -171± 19
N4(29)			.53 -172± 51	.92 11.8± 12	.61 -174± 40	.75 14.8± 26
N4(89)					.58 8.7±44	
N5(28)					.66 178± 34	.85 4.4± 18
N5(118)						.65 -177± 36

Table 3.6: Wavelength and phase speed calculated from θ, the phase estimate from the coherence calculation, for horizontal instrument pairs. A negative phase speed indicates phase propagation onshore.

WINTER

Instrument Pair	λ(km)	C_p(km/hr)
N3(32)-N4(29)	960	-52
N3(32)-N5(28)	910	-49
N3(32)-N6(10)	1100	-59
N4(29)-N5(28)	610	-33
N4(29)-N6(10)	990	-54
N5(28)-N6(10)	1700	-92

SUMMER

Instrument Pair	λ(km)	C_p(km/hr)
N1(10)-N2(10)	270	-15
N2(10)-N4(10)	470	-25
N2(32)-N3(32)	330	18
N4(10)-N5(10)	510	-28
N4(10)-N6(10)	2900	-160
N4(89)-N5(88)	7200	-390
N5(10)-N6(10)	7500	400

Table 3.7: Propagation characteristics across the southern extent of the array. A negative $\Delta\theta$ indicates that the seaward instrument appears to lead the shoreward instrument. The first column of numbers under each event represents values calculated assuming $c_p > 0$, i.e. phase propagation offshore, and wavelengths on the order of the mooring spacing. The second column represents values calculated assuming wavelengths much greater than the mooring spacing.

Between Instruments	Event # 1	2	3	4	5	6	7
N5(10)/N6(10)							
$\Delta\theta$ (degrees)	30	-15	15	*			
λ_H (km)	19,187	22,500	20,500				
c_p (km/hr)	1,10	1.2,-27	1.1,27				
N5(28)/N6(10)							
$\Delta\theta$ (degrees)					-22	*	*
λ_H (km)					22,500		
c_p (km/hr)					1.2,-27		
N4(10)/N5(10)							
$\Delta\theta$ (degrees)	-40	-20	*	*			
λ_H (km)	23,180	21,360					
c_p (km/hr)	1.2,-10	1.1,-19					
N4(29)/N5(28)							
$\Delta\theta$ (degrees)					*	*	*
λ_H (km)							
c_p (km/hr)							

* Phase lag is not stable to changes in piece length.

Table 3.8: Statistics of the current ellipses.

	SUMMER			WINTER		
Instrument	Rotary Coefficient	Ellipse Orientation	Ellipse Stability	Rotary Coefficient	Ellipse Orientation	Ellipse Stability
N1(10)	.83	110	.6			
N1(32)	.84	51	.2	.74	87	.28
N2(10)	.97	11	.53			
N2(32)	.96	147	.76	.95,.92	48,102	.32,.31
N2(52)	.88	27	.42	.99,.85	91,64	.09,.40
N2(65)	.88	97	.23	.96,.77	75,90	.22,.48
N3(10)					177	.33
N3(32)	.96	156	.15	.89	48	.39
N3(72)	.97	81	.46	.96	16	.39
N4(10)	.99	175	.40			
N4(29)				.97	103	.27
N4(59)	.96	81	.46			
N4(89)	.98	110	.11	.98	54	.38
N5(10)	.97	86	.20			
N5(28)	.98	17	.16	.98	125	.35
N5(88)	.98	134	.30			
N5(118)	.98	144	.24	.96	15	.27
N5(183)	.96	166	.64			
N6(10)	.99	40	.34	.99	136	.24

Table 4.1: Monthly average surface heat flux, computed from 32 years of data (Goldsmith and Bunker, 1979).

Month	Q[W/m^2]
January	-320
February	-290
March	-210
April	- 81
May	32
June	65
July	97
August	48
September	- 65
October	-180
November	-290
December	-360

Table 4.2: Comparison of two estimates of mixed layer depth at N4 and N5. h is the value extrapolated from available hydrographic sections. h* is calculated from upper and lower layer velocities by assuming that the velocities satisfy the ratio upper:lower = (H - h):h, where it is the total depth and h is the mixed layer depth.

	EVENT #						
	1	2	3	4	5	6	7
h[m]	>15	15	25	10	30	40	50
N5							
h*[m]	37	42	42	28	48	63	104
N4							
h*[m]	42	31	39	26	48	47	49

APPENDIX

Consideration of the critical frequency for the bottom slope at the NSFE array:

It is possible to estimate whether the bottom slope at the location of the NSFE array is supercritical for downard-propagating near-inerital internal waves. The bottom slope between moorings 5 and 6 is approximately $\alpha = 60$ m/6.25 km $= 9.6 \times 10^{-3}$ and between moorings 4 and 5 is approximately $\alpha = 20$ m/12.5 km $= 1.6 \times 10^{-3}$. Very roughly, the hydrographic sections taken during NSFE suggest that the buoyancy frequency N near the bottom should fall between two extremes -- a change of 1 kg/m^3 over 50 m or a change of 1 kg/m^3 over 100 m, corresponding to $9.7 \times 10^{-5} s^{-2} < N^2 < 1.9 \times 10^{-4} s^{-2}$. The bottom slope will be reflective if the frequency of the wave ω satisfies (LeBlond and Mysak, 1978):

$$f^2 < \omega^2 < (\alpha^2 N^2 + f^2)/(1 + \alpha^2),$$

or, if $\alpha^2 << 1$

$$1 < \omega^2/f^2 < \alpha^2 N^2/f^2 + 1.$$

For the lower value of N^2, and using $f = .0535$ cph to correspond to the value of the local inertial frequency at the southernmost extent of the array, $\sqrt{(\alpha^2 N^2/f^2 + 1)} \simeq 1.01$ over the outer shelf and $\sqrt{(\alpha^2 N^2/f^2 + 1)} \simeq 1.42$ over the slope. The slope will always be supercritical for frequencies in the inertial band, and with a conservative estimate of N^2, the outer shelf will be supercritical for frequencies up to approximately 1% above f. If the upper limit of N^2 is used, the outer shelf becomes supercritical to frequencies up to approximately 3% above f.